50th AIAA Aerospace Sciences Meeting including the New Horizons Forum and Aerospace Exposition
09 - 12 January 2012, Nashville, Tennessee
AIAA 2012-1025

Numerical Simulation of Nanosecond-Pulse Electrical Discharges

Jonathan Poggie* and Nicholas J. Bisek†
Air Force Research Laboratory, Wright-Patterson AFB, Ohio 45433-7512 USA
Igor V. Adamovich‡ and Munetake Nishihara§
The Ohio State University, Columbus, Ohio 43210 USA

Numerical calculations were carried out to examine the physics of the operation of a nanosecond-pulse, single dielectric barrier discharge in a configuration with planar symmetry. This simplified configuration was chosen as a vehicle to develop a physics-based nanosecond discharge model, including realistic air plasma chemistry and compressible bulk gas flow. First, a reduced plasma kinetic model (15 species and 42 processes) was developed by carrying out a sensitivity analysis of zero-dimensional plasma computations with an extended chemical kinetic model (46 species and 395 processes). Transient, one-dimensional discharge computations were then carried out using the reduced kinetic model, incorporating a drift-diffusion formulation for each species, a self-consistent computation of the electric potential using the Poisson equation, and a mass-averaged gas dynamic formulation for the bulk gas motion. Discharge parameters (temperature, pressure, and input waveform) were selected to be representative of recent experiments on bow shock control with a nanosecond discharge in a Mach 5 cylinder flow. The computational results qualitatively reproduce many of the features observed in the experiments, including the rapid thermalization of the input electrical energy and the consequent formation of a weak shock wave. At breakdown, input electrical energy is rapidly transformed (over roughly 1 ns) into ionization products, dissociation products, and electronically excited particles, with subsequent thermalization over a relatively longer time-scale (roughly 10 μs). The motivation for this work is modeling nanosecond-pulse, dielectric barrier discharges for applications in high-speed flow control. The effectiveness of such devices as flow control actuators depends crucially on the rapid thermalization of the input electrical energy, and in particular on the rate of quenching of excited electronic states of nitrogen molecules and oxygen atoms and on the rate of electron-ion recombination.

I. Introduction

Interest in plasma-based flow control dates to the mid-1950s, when magnetohydrodynamic reentry heat shields were first investigated.[1,2] Activity in the research area waned in the 1970s, with some work on drag reduction using corona discharges appearing in the 1980s.[3] A resurgence in the field took place in the 1990s, with the introduction of dielectric barrier discharge (DBD) actuators,[4] a revisit of reentry magnetohydrodynamics,[5] and the disclosure of the AJAX hypersonic vehicle concept.[6] In the fifteen years since this resurgence, plasma-based flow control techniques have been a topic of ongoing research, motivated by the possibility of extremely rapid actuation, a low-profile configuration, and the ability to operate in hostile environments.[7–17]

In the high-speed regime, plasma-based flow control devices have suffered the drawbacks of either excessive weight[18] or insufficient control authority.[4] Pulsed discharge devices, based on either arc[19] or glow discharges,[20] seem to be a promising way around these difficulties. Nanosecond-scale pulsed glow discharges

*Team Leader, High-Speed Flow Research Group, Computational Aerophysics Branch. Associate Fellow AIAA.
†Research Aerospace Engineer, High-Speed Flow Research Group, Computational Aerophysics Branch. Member AIAA.
‡Professor, Nonequilibrium Thermodynamics Laboratories, Dept. of Mechanical Engineering. Associate Fellow AIAA.
§Postdoctoral Researcher, Nonequilibrium Thermodynamics Laboratories, Dept. of Mechanical Engineering. Member AIAA.

Report Documentation Page

Form Approved
OMB No. 0704-0188

1. REPORT DATE	2. REPORT TYPE	3. DATES COVERED
JAN 2012		**00-00-2012 to 00-00-2012**

4. TITLE AND SUBTITLE	5a. CONTRACT NUMBER
Numerical Simulation of Nanosecond-Pulse Electrical Discharges	5b. GRANT NUMBER
	5c. PROGRAM ELEMENT NUMBER
6. AUTHOR(S)	5d. PROJECT NUMBER
	5e. TASK NUMBER
	5f. WORK UNIT NUMBER
7. PERFORMING ORGANIZATION NAME(S) AND ADDRESS(ES) **Air Force Research Laboratory,Wright Patterson AFB,OH,45433-7512**	8. PERFORMING ORGANIZATION REPORT NUMBER
9. SPONSORING/MONITORING AGENCY NAME(S) AND ADDRESS(ES)	10. SPONSOR/MONITOR'S ACRONYM(S)
	11. SPONSOR/MONITOR'S REPORT NUMBER(S)

12. DISTRIBUTION/AVAILABILITY STATEMENT
Approved for public release; distribution unlimited

13. SUPPLEMENTARY NOTES

14. ABSTRACT

15. SUBJECT TERMS

16. SECURITY CLASSIFICATION OF:			17. LIMITATION OF ABSTRACT	18. NUMBER OF PAGES	19a. NAME OF RESPONSIBLE PERSON
a. REPORT **unclassified**	b. ABSTRACT **unclassified**	c. THIS PAGE **unclassified**	**Same as Report (SAR)**	**26**	

are efficient generators of both ions and electronically excited molecules because of the extremely high instantaneous reduced electric field.[21]

The generation of shock waves by volumetric heat release in pulsed discharges was observed and explained in the 1970s in the context of gas laser technology.[22,23] Early computations by Aleksandrov et al.[23] assumed that all the power dissipated in the discharge immediately went into heating the neutral gas. Popov,[25] however, has emphasized a two-stage heating mechanism in which product species and electronically excited species are generated by electron impact, and then the stored chemical energy is converted to thermal energy through quenching reactions. Two-dimensional calculations have been carried out recently by Unfer and Boeuf,[24] assuming instant thermalization of 30% of the dissipated power going into electronic excitation.

In recent experiments,[17,26] control of a Mach 5 cylinder flow was demonstrated using a pulsed surface dielectric barrier discharge. Schematics of the experiment are shown in Fig. 1. Figure 1a shows a diagram of the model mounted in the wind tunnel, and Figs. 1b-c illustrate the actuator configuration on the cylinder.

The hollow cylinder model was made of fused quartz, with a 6 mm outside diameter and a 2 mm thick wall. A thin copper exposed electrode (12 mm $\times$ 1.5 mm $\times$ 0.1 mm) was affixed to the surface of the cylinder, with a second copper electrode mounted inside (a 3 mm diameter tube, 0.35 mm thick and 10 mm long). DuPont^{TM} Kapton® polyimide film was placed over the ends of the exposed electrode, leaving a 10 mm span exposed to the flow.

A combination of positive and negative polarity pulses to the two electrodes produced a potential difference of about 27 kV, lasting on the order of 5 ns (pulse full-width at half maximum). The effects of the energy release in the resulting discharge were captured using phase-locked schlieren imaging. Side-view schlieren images are shown in Fig. 2 for several time-delays after the discharge. A weak shock wave is seen to form near the edge of the exposed electrode, and propagate upstream in the shock-layer flow on a time scale on the order of microseconds. When it reaches the bow shock, the shock shape is altered, and the shock standoff increases by up to 25%. Given the close relationship between shock standoff and gradients at the stagnation point,[9] this system might be able to alter heat transfer rates at the nose of blunt body flows. Further, the system is promising for general high-speed flow control applications, for example control of supersonic inlet flows.[27]

We have begun to formulate a high-fidelity physical model of the energy transfer process in the pulsed surface dielectric barrier discharge.[28] For simplicity in the present work, we have focused on a planar geometry, where experimental evidence exists that a nearly one-dimensional discharge can occur at relatively low pressures.[29] (In a companion project, we are exploring the three-dimensional fluid mechanics of the experiment using a gasdynamics code with a phenomenological volumetric energy deposition model.[30]) Using coupled modeling of the plasma and compressible flow in a one-dimensional geometry, we plan to study the dominant physical effects, including energy thermalization kinetics and compression wave formation and propagation.

To this end, a reduced plasma kinetic model (15 species and 42 processes) was developed first by carrying out a sensitivity analysis of a zero-dimensional plasma computation with an extended chemical kinetic model (46 species and 395 processes). Transient, one-dimensional discharge computations were then carried out using the reduced kinetic model, incorporating a drift-diffusion formulation for each species, a self-consistent computation of the electric potential using the Poisson equation, and a mass-averaged gas dynamic formulation for the bulk gas motion.

II. Development of Reduced Kinetic Model

To obtain the reduced kinetic model, we applied a sensitivity analysis to a detailed, transient, zero-dimensional air plasma model used in previous work.[31] The reduced model was developed to identify the dominant species and reactions affecting the energy balance and the rate of thermalization in the discharge, and to minimize the computational cost of the transient, one-dimensional calculations that will be presented in Sec. III.

The full air plasma model is based on the model developed by Kossyi et al.[32] It incorporates a set of ordinary differential equations for number densities of neutral species N, N_2, O, O_2, O_3, NO, NO_2, N_2O, NO_3, charged species e^-, N^+, N_2^+, N_3^+, N_4^+, O^+, O_2^+, O_4^+, NO^+, NO_2^+, N_2O^+, $N_2O_2^+$, N_2NO^+, O_2NO^+, $NONO^+$, O^-, O_2^-, O_3^-, NO^-, NO_2^-, NO_3^-, N_2O^-, and excited species $N_2(A^3\Sigma)$, $N_2(B^3\Pi)$, $N_2(C^3\Pi)$, $N_2(a'^1\Sigma)$, $O_2(a^1\Delta)$, $O_2(b^1\Sigma)$, $O_2(c^1\Sigma)$, $N(^2D)$, $N(^2P)$, $O(^1D)$ produced in the plasma, as well as an energy equation for predicting the time evolution of gas temperature. This set of equations is coupled with a steady,

two-term expansion of the Boltzmann equation for the electron energy distribution function (EEDF) of the plasma electrons.[33] These calculations employ experimental cross sections of electron impact electronic excitation, dissociation, ionization, and dissociative attachment processes.[34,35] The rate coefficients of these electron impact processes, as functions of the reduced electric field E/N, are derived from the Boltzmann solutions by averaging the cross sections over the EEDF. The model also incorporates chemical reactions of ground state species and excited electronic species, electron-ion recombination and ion-ion neutralization processes, ion-molecule reactions, and electron attachment and detachment processes. The rate coefficients of these processes are taken from Kossyi et al.[32] The air plasma processes and the kinetic rates used are listed in a previous paper.[31]

In the zero-dimensional modeling calculations using the full air plasma kinetic model, the time-resolved reduced electric field (i.e. the pulse voltage waveform) was one of the inputs for the model. The voltage waveform was approximated as a pulse with Gaussian form, $U(t) = U_{\text{peak}} \exp[-(t-t_0)^2/\tau^2]$, where U_{peak} is the peak voltage, t_0 is the moment when the voltage peaks, and $\tau = 3$ ns is the pulse width parameter. The pulse width parameter was chosen to fit the experimental voltage pulse duration produced by a nanosecond pulse generator (FID GmbH, FPG 60-100MC4) with pulse full-width half-maximum of 5 ns.[26]

The pulse peak voltage was considered an adjustable parameter, and varied to produce discharge pulse energy loading of 50-100 meV/molecule. At these conditions, if all discharge input energy were thermalized, the resultant temperature rise in the discharge would be $\Delta T \sim$ 165-330 K (thermalization of 1 meV/molecule input energy corresponds to $\Delta T = 3.32$ K). However, recent kinetic modeling calculations and experiments[25,36,37] suggest that approximately 30% of the input energy is thermalized rapidly after a discharge pulse with a peak reduced electric field of $(E/N)_{\text{peak}} =$ 200-900 Td (1 Td $= 10^{-17}$ V-cm^2), during collisional quenching of electronically excited species.

Calculations and experiments by Aleksandrov et al.[38] suggest that in nanosecond pulse discharges at atmospheric pressure at very high values of the reduced electric field, $E/N \sim 1000$ Td, the rapidly thermalized energy fraction increases up to about 50%, due to contributions of ion-molecule reactions, electron-ion recombination, and ion-ion recombination. The time scale for the rapid energy thermalization ranges from a few microseconds at $p \sim 0.01$ atm[37] to below one microsecond at $p \sim 1$ bar.[38] This effect would limit the temperature rise due to rapid energy thermalization after the discharge pulse to $\Delta T \sim$ 50-100 K. This is consistent with the temperature rise measured in a single-pulse nanosecond surface dielectric barrier discharge (SDBD) in dry air at $p \sim 30$ Torr using the FID pulse generator, $\Delta T = 40 \pm 30$ K[26] and in a single-pulse nanosecond SDBD in room air using a custom-designed nanosecond pulse generator, $\Delta T = 80 \pm 50$ K.[39]

In the present paper, our primary objective is to study the effect of rapid energy thermalization on compression wave formation in the discharge, for a time scale after the discharge pulse shorter than the acoustic time $\tau_{\text{acoustic}} = L/a$. (Here L is the characteristic size of the plasma and a is the local speed of sound.) Strong compression waves generated by nanosecond-pulse discharges can be used for high-speed flow control. Nanosecond-gate, broadband ICCD images of nanosecond-pulse surface dielectric barrier discharges[17,26] have shown that the thickness of the near-surface plasma layer at atmospheric pressure is of the order of 100 μm, which corresponds to an acoustic time of $\tau_{\text{acoustic}} \sim 0.3$ μs. Thus, nanosecond-pulse discharge energy thermalization on a shorter time scale at atmospheric pressure would result in strong compression wave formation, as detected in experiments.[17,20,39,40]

Transient, zero-dimensional calculations have been conducted for a single-pulse discharge in dry air at pressures ranging from 30 Torr to 760 Torr, initially at room temperature. Since peak reduced electric field in these calculations varied from $(E/N)_{\text{peak}} \sim 600$ Td (at $p = 30$ Torr) to $(E/N)_{\text{peak}} \sim 200$ Td (at $p = 760$ Torr), vibrational excitation by electron impact was neglected. For $E/N > 200$ Td, discharge energy fraction loaded into the vibrational energy mode of nitrogen does not exceed 10%. Heat transfer from the gas heated in the discharge was also neglected. Using sensitivity analysis, a reduced kinetic model incorporating 15 species (N_2, O_2, O, O_3, NO, N, $O(^1D)$, $N_2(A^3\Sigma)$, $N_2(B^3\Pi)$, $N_2(a'^1\Sigma)$, $N_2(C^3\Pi)$, e^-, N_2^+, O^+, O_2^+) and 42 processes was obtained from the full air plasma model including 46 species and 395 processes (see Tables 1-2). Since, at the high peak reduced-electric-fields involved here, the rate of electron impact ionization greatly exceeds the rate of electron attachment, processes involving negative ions do not affect the energy balance. During the sensitivity analysis, the main criterion used was the effect of individual processes on time-dependent energy fraction thermalized after the discharge pulse. The results of calculations for $p = 30$ Torr are summarized in Figs. 3-6, and for $p = 760$ Torr in Figs. 7-10.

From Fig. 3, it can be seen that at $p = 30$ Torr, peak reduced electric field and peak ionization fraction are approximately $(E/N)_{\text{peak}} = 580$ Td and $(ne/N)_{\text{peak}} = 8 \times 10^{-4}$ ($n_e = 7.7 \times 10^{14}$ cm^{-3}), respectively.

Figure 4 shows that energy fraction thermalized during the first 10 μs after the pulse is approximately 31%. Comparing Figs. 4 and 5 demonstrates that the energy thermalization on this time scale is primarily due to collisional quenching of $N_2(A^3\Sigma)$, $N_2(B^3\Pi)$, $N_2(a'^1\Sigma)$, $N_2(C^3\Pi)$, and $O(^1D)$, as well as electron-ion recombination. Further energy thermalization, on a much longer time scale of 10 μs to 100 ms, occurs primarily in reactions of nitrogen and oxygen atoms with oxygen molecules, $N + O_2 \rightarrow NO + O$ and $O + O_2 + M \rightarrow O_3 + M$, resulting in nitric oxide and ozone formation, as well as in reaction $O + O_3 \rightarrow O_2 + O_2$. Figure 4 also demonstrates the accuracy of the reduced kinetic model as compared to the full model.

The results obtained at $p = 760$ Torr are shown in Figs. 7-10. In this case, both peak reduced electric field and peak ionization fraction are lower, $(E/N)_{\text{peak}} = 200$ Td and $(ne/N)_{\text{peak}} = 2 \times 10^{-4}$ ($n_e = 4.9 \times 10^{15}$ cm^{-3}), respectively (see Fig. 7). From Fig. 8, it can be seen that energy fraction thermalized within 1 μs after the pulse is approximately 23%. Again, energy thermalization on this time scale is due to collisional quenching of $N_2(A^3\Sigma)$, $N_2(B^3\Pi)$, $N_2(a'^1\Sigma)$, $N_2(C^3\Pi)$, and $O(^1D)$ (compare Figs. 8 and 9), followed by an additional 25% of input energy thermalized on a long time scale, 1-300 μs after the pulse, in chemical reactions of nitric oxide and ozone formation. The reduced kinetic model obtained based on the modeling results at $p = 30$ Torr remains accurate (see Fig. 8).

The rest of the zero-dimensional modeling calculations were consistent with the low-pressure and the high-pressure cases shown in Figs. 3-10. For the entire pressure range tested, $p = 30 - 760$ Torr, the rapidly thermalized discharge energy fraction was in the range of 25-30%. The time scale for rapid energy thermalization, predicted by the model, varies from 2-3 μs at $p = 30$ Torr to 0.2-0.3 μs at $p = 760$ Torr (e.g., see Figs. 4 and 8). Thus, rapid heating after a discharge pulse coupling 100 meV/molecule to dry air would result in localized heating by 80-100 K.

Rate coefficients of electron impact processes incorporated into the reduced kinetic model, predicted by the Boltzmann equation solver and approximated as functions of the reduced electric field, are listed in Table 2. These rates, as well as rate coefficients of chemical reactions, excited electronic species quenching, and electron-ion recombination, have been used in the coupled electric discharge / compressible flow model to predict heating and compression wave formation in a nanosecond-pulse discharge in a geometry with planar symmetry.

III. Discharge Computations

The 15-species reduced kinetic model was applied to transient, one-dimensional discharge computations. The following models were employed to predict particle motion: a drift-diffusion formulation for the charged particles, a diffusion equation for the neutrals, and a mass-averaged fluid formulation for the bulk gas. The Poisson equation was solved for the electric potential. A detailed description of the overall physical model is given below.

For computational efficiency, the calculations were carried out in two stages. The first stage encompassed the period in which an external waveform was applied to the electrodes. For this stage, the full physical model was employed. Shortly after the external potential was turned off, electromagnetic effects and charged particle motion became negligible. In this second stage of the problem, we set the electric field to zero, and imposed neutrality by setting the electron number density to an appropriate value.

A. Governing Equations

A drift-diffusion formulation was used for the charged particles:

$$\frac{\partial n_s}{\partial t} + \nabla\cdot(n_s\mathbf{w} \pm n_s\mu_s\mathbf{E} - D_s\nabla n_s) = \omega_s \tag{1}$$

and a diffusion formulation was used for the neutrals:

$$\frac{\partial n_s}{\partial t} + \nabla\cdot(n_s\mathbf{w} - D_s\nabla n_s) = \omega_s \tag{2}$$

Here the electric field is $\mathbf{E} = -\nabla\phi$, where ϕ is the electric potential. The subscript s indicates the species number. For each species-s, the number density is n_s, the mobility is μ_s, the diffusion coefficient is D_s, and the rate of production in reactions is ω_s. The bulk fluid velocity is $\mathbf{w}$.

A mass-averaged fluid dynamic formulation was used to model the motion of the gas as a whole:

$$\begin{aligned} \frac{\partial \rho}{\partial t} + \nabla\cdot(\rho\mathbf{w}) &= 0 \\ \frac{\partial}{\partial t}(\rho\mathbf{w}) + \nabla\cdot(\rho\mathbf{w}\mathbf{w} + p\mathbf{I}) &= \nabla\cdot\tau + \zeta\mathbf{E} \\ \frac{\partial}{\partial t}[\rho(\epsilon + w^2/2)] + \nabla\cdot[\rho\mathbf{w}(\epsilon + w^2/2) + p\mathbf{w}] &= \nabla\cdot(\tau\cdot\mathbf{w} - \mathbf{Q}) + \mathbf{E}\cdot\mathbf{j} \end{aligned} \tag{3}$$

Here ρ is the mass density, p is the pressure, τ is the viscous stress tensor, ζ is the space charge, $\mathbf{j}$ is the total electric current, ϵ is the internal energy, $\mathbf{Q}$ is the heat flux. It useful to also define the dissipated power $P = \mathbf{E}\cdot\mathbf{J}$, where $\mathbf{J} = \mathbf{j} - \zeta\mathbf{w}$.

The relationship between the species properties and the overall properties are as follows:

$$\begin{aligned} \rho &= \sum_s m_s n_s & p &= \sum_s p_s \\ \rho\epsilon &= \sum_s m_s n_s \epsilon_s & \rho\mathbf{w} &= \sum_s m_s n_s \mathbf{v}_s \\ \zeta &= \sum_s q_s n_s & \mathbf{j} &= \sum_s q_s n_s \mathbf{v}_s \end{aligned} \tag{4}$$

where the mass per particle is m_s, the charge per particle is q_s, the partial pressure is $p_s = n_s k_B T$, and the species internal energy is $\epsilon_s = h_s^0 + C_{v,s}T$. Further, the laboratory-frame species velocity is $\mathbf{v}_s = \mathbf{w} \pm \mu_s\mathbf{E} - (D_s\nabla n_s)/n_s$.

The viscous stress and heat flux are as follows:

$$\begin{aligned} \tau &= \mu_v\left[(\nabla\mathbf{w}) + (\nabla\mathbf{w})^T - \tfrac{2}{3}\nabla\cdot\mathbf{w}\mathbf{I}\right] \\ \mathbf{Q} &= -k\nabla T + \sum_s \rho_s \mathbf{U}_s h_s \end{aligned} \tag{5}$$

where μ_v is the viscosity, k is thermal conductivity, $\mathbf{U}_s = \mathbf{v}_s - \mathbf{w}$ is the diffusion velocity, and $h_s = \epsilon_s + p_s/\rho_s$ is the species enthalpy.

Given the very high diffusion velocities in the cathode layer of a nanosecond-pulse discharge, careful consideration must be made of the validity of a formulation based on the mass-averaged global conservation laws. The mass averaged formulation assumes, for example, that the species internal energy is the same for the mass-averaged reference frame as for the species reference frame. In the Appendix, we show that the formulation used here is valid as long as the kinetic energy associated with diffusion is small compared to the mixture internal energy. For the present work, this ratio is at most $\frac{1}{2}n_s m_s U_s^2/(\rho\epsilon) \sim 10^{-3}$, so the model is well justified.

The Poisson equation is employed to compute the electric potential:

$$\nabla^2\phi = -\zeta/\epsilon_0 \tag{6}$$

where ϵ_0 is the permittivity of free space.

B. Gas Properties and Boundary Conditions

The 15-species, 42-process formulation described previously was employed, including neutrals, ions, electrons, and electronically-excited species (Tables 1-2). Data for mobility and diffusion coefficient for each species of heavy particle were take from the literature.[13,41–43] Correlations of electron temperature and electron mobility with reduced electric field (Fig. 11) were developed from the Boltzmann equation solutions described in Sec. II. The viscosity and thermal conductivity of the bulk gas were based on standard correlations for air.[44]

A one-dimensional computational domain was employed to represent a single dielectric barrier discharge (Fig. 12). No-slip boundary conditions with a constant temperature wall were employed for the bulk gas. A zero wall-normal derivative was imposed for the neutral species.

Standard boundary conditions were employed for the charged particles. First, the conditions at the wall were determined by setting the normal derivative to zero. Then, if the provisional ion flow was away from

the boundary, the ion flux was set to zero. The electron number density was determined through a balance between the kinetic flux to the wall and secondary emission. For certain cases, these boundary conditions led to numerical instability at the exposed electrode boundary (anode). When this occurred, the simplified boundary conditions described in Ref. 45 were employed.

For the bare electrode the potential was specified as zero (grounded). An alternative boundary condition was employed for the powered electrode with a dielectric coating (see also Ref. 46). The dielectric layer was assumed to be sufficiently thin that a linear potential profile (uniform electric field $\mathbf{E}_d$) was a good approximation. The electric field inside the dielectric was related to the electric field $\mathbf{E}$ at the surface through the relation $\epsilon_0\mathbf{E}-\epsilon_r\epsilon_0\mathbf{E}_d = \sigma\mathbf{n}$, where σ is the surface charge density and $\mathbf{n}$ is the unit normal vector pointing into the computational domain. The surface charge was determined by integrating $\partial\sigma/\partial t = -\mathbf{j}\cdot\mathbf{n}$ for each surface point, using a time-marching scheme analogous to that of the main governing equations.

C. Numerical Methods

The calculations were carried out using the Air Force Research Laboratory code HOPS (Higher Order Plasma Solver).[47–50] The code includes several physical models and numerical schemes. Here, the physical model consisting of Eqs. (1)-(3) and (6) was solved using an implicit, second-order, upwind formulation. All the equations were solved in a nondimensional form that has been described in previous papers.[47–50]

Time integration of the conservation equations (1)-(3) was carried out using a second-order implicit scheme, based on a three-point backward difference of the time terms. The formulation is similar to the standard technique of Beam and Warming,[51] but adapted to a multi-fluid formulation with different models for particle motion.

Approximate factoring and quasi-Newton subiterations were employed. The implicit terms were linearized in the standard 'thin layer' manner. The implicit terms were evaluated with second-order spatial accuracy, yielding a block tridiagonal system of equations for each factor. The species were loosely coupled, limiting the rank of the flux Jacobian matrices to the order of the moment model (one for the drift-diffusion formulation, five for the overall conservation equations). Each factor was solved in turn using a standard block tridiagonal solver, and the change in the solution vector of conserved variables was driven to zero by the subiteration procedure at each time step. Three applications of the flow solver per time-step were employed for the present work.

For the mass-averaged fluid model employed for the bulk gas, the Roe scheme[52,53] was employed for the inviscid fluxes. For the drift-diffusion model, a simple upwinding scheme was employed, based on the convection-drift velocity. This is similar to the approach of Surzhikov and Shang.[45] In both formulations, stability was enforced using the minmod limiter in the MUSCL formalism.[54]

The Poisson equation (6) was solved at the end of each sub-iteration in the implicit time-marching scheme. (Using this strategy with the subiteration procedure gives about the same improvement in stable time-step as methods based on the linearization of the right-hand-side of the Poisson equation.[55]) An approximately factored implicit scheme was employed, adapted from the approach described by Holst.[56] The formulation of the implicit scheme was analogous to that of the conservation equations, with linearization of the implicit terms, approximate factoring, and an iterative procedure that drives the change in the solution to zero. The spatial derivatives were evaluated using second-order central differences, and the system was solved using the Thomas tridiagonal algorithm.[57]

As mentioned earlier, the calculations were carried out in two phases. The first stage of the calculations encompassed the first 100 ns of the discharge, and employed the full physical model discussed above, Eqs. (1)-(3) and (6). Since electromagnetic effects and charged particle motion became negligible after the input pulse died away (after about 24 ns), in the second stage of the computations (0.1 μs to 100.1 μs), the electric field was set to zero and neutrality was enforced by appropriately setting the electron number density. This approach resulted in a substantial savings in computational cost.

For the calculations presented here, a uniform grid of 1001 points across the gap was employed. Grid resolution studies presented in a previous paper[28] indicate that this level of grid resolution is sufficient for this problem. The time step used for the Phase 1 calculations was 1 ps, and the time-step for Phase 2 was 5 ns.

D. Results

In the experiments illustrated in Figs. 1-2, typical freestream conditions for the neutral gas were a speed of 715 m/s, a pressure of 159.5 Pa, and a temperature of 56 K. Sample calculations are presented here for a one-dimensional discharge under conditions representative of the stagnation region of the cylinder flow experiment. The corresponding stagnation conditions, computed using the Rayleigh supersonic Pitot formula[58] were 4.74 kPa (36 Torr) and 310.3 K. For each case in the calculations discussed below, the initial, uniform state of the neutral gas was set to these stagnation values.

The configuration considered here is illustrated in Fig. 12. The problem is one-dimensional. In the simulations, the right electrode was grounded and the left electrode, which was coated with a thin dielectric layer, was powered with the input signal $V_s = -V_0 \exp\left[-(t-t_0)^2/\tau^2\right]$. For the present calculations, we assumed $V_0 = 20$ kV, $\tau = 3$ ns, and $t_0 = 12$ ns.

The discharge gap was taken to be 10 mm. The initial mole fraction of the electrons and each of the neutral minor species was taken to be 1×10^{-10}. The mole fraction for each ion species was equal, and set so that the space charge was zero. The initial electric field was zero. The dielectric coating was assumed to be 2 mm thick, with a relative dielectric constant of $\epsilon_r = 3.8$, chosen to be representative of fused quartz. The secondary emission coefficient was $\gamma_{\text{sem}} = 0.05$.

A previous paper[13] presented an analytical model of nanosecond-pulse dielectric barrier discharges, in which an electron-free sheath region was coupled to a uniform, quasi-neutral plasma region. The model provided closed-form expressions for the discharge properties, and displayed good agreement with experiment. We employ this model here to provide a basic check of the correctness of our computer code, and to introduce the general features of the nanosecond-pulse discharge in one dimension. Figure 13 compares the discharge properties in the plasma predicted by this analytical model and by the one-dimensional computations. Note that $t_0 = 100$ ns for the analytical model, but $t_0 = 12$ ns for the numerical computations.

Figures 13a-b show the applied electric field (field in the absence of plasma), the computed field, and the ionization fraction. Some quantitative differences are present, but the general shape of the curves is in agreement. Because of the shielding effect of space charge in the cathode sheath and surface charge accumulation on the dielectric, the field in the plasma is less than the applied field. The one-dimensional computations predict a peak electric field at 9.4 ns, before the input pulse maximum at 12 ns, followed by a smaller peak of opposite sign at 14.5 ns. The peak electron mole fraction reaches about 2×10^{-6}.

Figures 13c-d show the reduced electric field E/N, the dissipated power $\mathbf{E} \cdot \mathbf{J}$, and the increase in gas energy density $\Delta(\rho\epsilon)$ (including chemical and thermal energy). Again, the results are qualitatively consistent between the two models, with moderate quantitative differences.

For the one-dimensional numerical computations, the peak reduced electric field is about 750 Td. Peak dissipated power (1.0×10^{11} W/m^3) occurs as the reduced electric field in the plasma is rapidly falling, but before the peak in the applied electric field. The analytical model predicts a total energy transferred to the gas of about 0.70 meV/molecule, whereas the numerical computations predict about one-third of this value (0.2 meV/molecule or 38 J/m^3). This difference is primarily due to the use of different expressions for the ionization rate coefficient as a function of reduced electric field in the analytical model and the present numerical computations. If the same expressions for ionization rate are used in the analytical model and the numerical simulations, the agreement for the predicted pulse energy coupled to the plasma improves considerably (see Ref. 13).

Recall that for the corresponding zero-dimensional computations discussed in Sec. II (Figs. 3-6), a discharge energy loading on the order of 100 meV/molecule was required to replicate the experimental results, with about 30 meV/molecule thermalized with 0.1 ms. In the present one-dimensional calculations, we obtained a discharge energy loading of about 0.2 meV/molecule in the plasma. The plasma electric field is comparable for the two the formulations (580 Td for zero-dimensional vs. 750 Td for one-dimensional), but the ionization fraction in the plasma is two orders of magnitude higher for the zero-dimensional calculations (8×10^{-4} vs. 2×10^{-6}).

The discrepancy between the predictions of the two models occurs because of plasma self-shielding in the one-dimensional calculations. This effect rapidly reduces the electric field in the plasma and limits the peak electron density. The results demonstrate that using zero-dimensional plasma kinetic modeling, with an imposed voltage waveform, is not appropriate even in a simple, symmetric configuration, since it greatly overestimates both peak electron density and energy coupled to the plasma.

Figure 14 shows discharge profiles at several stages in the computations. The species are grouped: the profiles of the total number densities of all ions (N_2^+ , O_2^+, and O^+), electrons (e^-), excited neutrals

($N_2(A^3\Sigma)$, $N_2(B^3\Pi)$, $N_2(a'^1\Sigma)$, $N_2(C^3\Pi)$, and $O(^1D)$), and ground-state neutrals (O, O_3, NO, N) are shown. The concentrations of N_2 and O_2 remain almost constant, and are omitted. The onset of breakdown and appearance of the peak reduced electric field are illustrated in Figs. 14a-b (9-10 ns). The sheath forms rapidly at the left (covered) electrode, is about 1 mm thick, and carries most of the potential drop across the gap. Most of the production of new species occurs near the sheath edge and in the plasma. At later stages in the computation (Fig. 14c, 14 ns), the electric field reverses sign in the plasma (see also Ref. 21), with an accompanying local maximum in time of the field magnitude. At the end of first state of the calculations (Fig. 14d, 100 ns), quasi-neutrality prevails in the domain, and the electric field is negligible. Since diffusion has not had time to act, a number of local maxima are present in the species number density profiles. These appear to reflect the motions of the sheath edge.

Figure 15 shows the time-history in the plasma ($x = 8$ mm) of the mole fraction of each of the species except N_2 and O_2, which remain essentially constant. Results are shown for both the Phase 1 computations (0–0.1 μs, space charge included) and Phase 2 computations (0.1 μs–100.1 μs, zero electric field and neutrality imposed). The concentrations of charged and excited particles increase suddenly when the electric field becomes strong, and decrease gradually after the input waveform ends. The longest-lived species are O_2^+ and $N_2(A^3\Sigma)$. The radicals N and O appear at breakdown, whereas NO and O_3 increase gradually after the end of the input waveform.

We see from Fig. 15 that breakdown results in the rapid formation of new species, which gradually recombine over a longer time scale. Figure 16 addresses the accompanying energy redistribution. For a station in the quasi-neutral plasma ($x = 8$ mm), the distribution of chemical energy over different groups of species is shown in Fig. 16a, and the distribution between chemical and thermal energy is shown in Fig. 16b. Corresponding plots for a station near the sheath edge ($x = 1$ mm), are shown in Figs. 16c-d.

Through the dissipative power term $\mathbf{E} \cdot \mathbf{J}$, breakdown converts part of the input electric energy into chemical energy of new species over a time scale of about 1 ns, then recombination reactions convert the stored chemical energy to thermal energy over roughly a 10 μs time scale. Initially, most of the chemical energy is stored in charged particles and excited neutrals. With time, this energy thermalizes through electron-ion recombination and collisional quenching of electronically excited species. At the same time additional energy goes into neutral species in the ground electronic states (N, O, NO, and O_3), tending to reduce the efficiency of the device in rapidly converting electrical energy to heat.

In the plasma, most of the input energy is initially stored in chemical energy, whereas near the sheath edge this fraction is relatively small. In ongoing work, we are investigating how nonlocal effects and the uncertainty in reaction rates in this region of very high reduced electric field influence this result.

The oscillations in internal energy seen in Fig. 16c for times of 10-20 ns are related to the rapid motion of the sheath edge during that time interval. (See Fig. 14.)

Also shown in Figs. 16b and 16d is a comparison of the time-integral of the input power density $\int_0^t \mathbf{E} \cdot \mathbf{J}\, d\hat{t}$ to the change in total internal energy. For the plasma region, these are seen to agree almost exactly, indicating that the heating is essentially a zero-dimensional phenomenon: spatial gradient terms like convection and heat conduction act over much longer time scales. For the sheath region, however, fluid motion is seen to begin to carry away thermal energy within 100 ns.

The acoustic time scale mentioned previously is nicely illustrated in Figs. 16b and 16d: after several microseconds, acoustic waves form due to the rapid heating, creating the spikes apparent in the plots. Only energy that is released as heat on a time scale shorter than the acoustic time can contribute to the formation of these waves.

The acoustic waves are more apparent in Fig. 17, which shows the heating and gas motion induced by the discharge. The majority of the heating occurs near the edge of the cathode sheath, forming weak waves that travel across the domain. For example, consider the velocity profiles in Fig. 17b, and note the wave structure. Two waves, traveling in opposite directions, appear near $x = 1$ mm for the 0.1 μs profile (red curve). After 4.1 μs (green curve), the left-running wave has reflected off the left boundary and trails the other compression wave. Note also the growth in wave strength between these two times; the waves are driven by exothermic reactions in a manner analogous to a detonation.

For this case, the waves are relatively weak, with a peak gas velocity of about 3 m/s and peak temperature rise of about 11 K. The stationary background gas experiences less than a 1 K temperature rise over the time covered in the simulation. For an air temperature of 310.8 K, the speed of sound is about 353 m/s. Estimating the wave speed by measuring displacements in Fig. 17a, we find 355 m/s, which is very slightly supersonic.

Substantially supersonic wave speeds (up to 480 m/s) have been observed experimentally.[20] In ongoing work, we are attempting to replicate this stronger gasdynamic interaction by altering the simulation conditions to increase the coupled energy density.

IV. Summary and Conclusions

Numerical calculations were carried out to examine the physics of the operation of a nanosecond-pulse, single dielectric barrier discharge in a configuration with planar symmetry. This simplified configuration was chosen as a vehicle to develop a physics-based nanosecond discharge model, including realistic air plasma chemistry and compressible bulk gas flow. Discharge parameters (temperature, pressure, and input waveform) were selected to be representative of recent experiments on bow shock control with a nanosecond discharge in a Mach 5 cylinder flow.

First, a reduced plasma kinetic model (15 species and 42 processes) was developed by carrying out a sensitivity analysis of zero-dimensional plasma computations with an extended chemical kinetic model (46 species and 395 processes). Transient, one-dimensional discharge computations were then carried out using the reduced kinetic model, incorporating a drift-diffusion formulation for each species, a self-consistent computation of the electric potential using the Poisson equation, and a mass-averaged gas dynamic formulation for the bulk gas motion.

A grid converged solution and reasonable comparison to a validated analytical model indicate that the computations reflect an accurate solution of the mathematical model. The computational results qualitatively reproduce many of the features observed in experiments, including the rapid thermalization of the input electrical energy and the consequent formation of a weak shock wave. The results illustrate how input electrical energy is rapidly transformed (over roughly 1 ns) at breakdown into ionization products, dissociation products, and electronically excited particles, and how thermalization occurs over a relatively longer time-scale (roughly 10 μs).

The motivation for the present work is modeling nanosecond-pulse, dielectric barrier discharges for applications in high-speed flow control. The effectiveness of such devices as flow control actuators depends crucially on the rapid thermalization of the input electrical energy, and in particular on the rate of quenching of excited electronic states of nitrogen molecules and oxygen atoms and on the rate of electron-ion recombination.

Future work will include using the coupled nanosecond discharge / compressible flow model developed in the present work for simulation of surface nanosecond pulse discharges. The main difference of the present approach from other recent studies of nanosecond pulse discharges in air[24] is that the present model incorporates the kinetics of energy storage and thermalization.

In addition, various flow control applications will be explored. One option under consideration is replacing the cylinder model with a blunt oblique shock generator, and examining whether the nanosecond discharge can affect an impinging shock / boundary layer interaction. There is a strong motivation to control such interactions for supersonic engine inlet applications.[27]

Appendix: Mass-Averaged Conservation Equations

The present paper employs a mass-averaged formulation of the conservation laws for the gas as a whole, Eq. (3). Here we present a brief derivation of the mass-averaged formulation from the conservation laws for individual species, and discuss the range of applicability of the conventional mass-averaged formulation for our applications. (See also Ref. 59.)

A derivation of the conservation laws for the individual species, as moments of the Boltzmann equation, was presented in a previous paper,[49] and is also addressed elsewhere.[60–62] Briefly, the moment equations are obtained by multiplying the Boltzmann equation by a conserved quantity, and integrating over all velocity space. Considering a quantity $\phi(\mathbf{u})$ associated with each particle of species-s, an average value is defined as $\langle\phi\rangle_s(\mathbf{x},t) = \int \phi(\mathbf{u}) f_s(\mathbf{x},\mathbf{u},t)\, d^3u$, where where $\mathbf{u}$ is the particle velocity, f_s is the distribution function, and the integral is over all velocity space. The resulting the mass, momentum, and energy conservation equations

for species-s are:

$$\begin{aligned}
\frac{\partial \rho_s}{\partial t} + \nabla\cdot(\rho_s \mathbf{v}_s) &= S_s \\
\frac{\partial}{\partial t}(\rho_s \mathbf{v}_s) + \nabla\cdot(\rho_s \mathbf{v}_s \mathbf{v}_s + p_s \mathbf{I}) &= \nabla\cdot\tau_s + \rho_s \mathbf{g} + \zeta_s\left(\mathbf{E} + \mathbf{v}_s \times \mathbf{B}\right) + \mathbf{A}_s \\
\frac{\partial}{\partial t}\left[\rho_s\left(\epsilon_s + \tfrac{1}{2}v_s^2\right)\right] + \nabla\cdot\left[\rho_s \mathbf{v}_s\left(\epsilon_s + \tfrac{1}{2}v_s^2\right) + p_s \mathbf{v}_s\right] &= \\
\nabla\cdot[\tau_s\cdot\mathbf{v}_s - \mathbf{Q}_s] + \rho_s \mathbf{v}_s\cdot\mathbf{g} + \zeta_s \mathbf{v}_s\cdot\mathbf{E} + M_s &
\end{aligned} \tag{7}$$

where the mass density has been defined as $\rho_s = n_s m_s$ and the charge density as $\zeta_s = n_s q_s$. The mean velocity is defined as $\mathbf{v}_s = \langle \mathbf{u} \rangle_s$ and the peculiar velocity as $\mathbf{V}_s = \mathbf{u} - \mathbf{v}_s$. The source terms S_s, $\mathbf{A}_s$, and M_s represent the exchange between species of particle identity, momentum, and energy in collisions. Also defined are the:

$$\begin{aligned}
\text{Kinetic pressure: } & p_s = \tfrac{1}{3} n_s m_s \langle V_s^2 \rangle_s \\
\text{Thermal energy: } & \epsilon_s = \epsilon_{\text{int},s} + \tfrac{1}{2}\langle V_s^2 \rangle_s \\
\text{Viscous stress: } & \tau_s = -n_s m_s [\langle \mathbf{V}_s \mathbf{V}_s \rangle_s - \tfrac{1}{3}\langle V_s^2 \rangle_s \mathbf{I}] \\
\text{Heat flux: } & \mathbf{Q}_s = \mathbf{Q}_{\text{int},s} + \tfrac{1}{2} n_s m_s \langle \mathbf{V}_s\, V_s^2 \rangle_s
\end{aligned} \tag{8}$$

The terms $\epsilon_{\text{int},s}$ and $\mathbf{Q}_{\text{int},s}$ represent internal molecular energy and the transfer of such energy by diffusion (e.g., see Ref. 62).

The conservation of mass, momentum, and total energy in collisions requires that the sum over all species of each of the corresponding collision source terms is zero: $\sum_s S_s = 0$, $\sum_s \mathbf{A}_s = 0$, $\sum_s M_s = 0$. These properties can be used to relate the species conservation laws (7) to the conservation laws for the gas as a whole.

The overall density is defined as $\rho = \sum_s \rho_s$. Consider the alternative peculiar velocity $\mathbf{W} = \mathbf{u} - \mathbf{w}$, where $\mathbf{w} = \sum_s \rho_s \mathbf{v}_s / \rho$ is the mass-weighted average velocity. The species diffusion velocity is defined as $\mathbf{U}_s = \langle \mathbf{W} \rangle_s = \mathbf{v}_s - \mathbf{w}$. (Note that $\mathbf{W} = \mathbf{U}_s + \mathbf{V}_s$.) In the mass-average reference frame, the moment terms, analogous to Eq. (8), are:

$$\begin{aligned}
\tilde{p}_s &= \tfrac{1}{3}\rho_s \langle W^2 \rangle_s = p_s + \tfrac{1}{3}\rho_s U_s^2 \\
\tilde{\epsilon_s} &= \epsilon_{\text{int},s} + \tfrac{1}{2}\langle W^2 \rangle_s = \epsilon_s + \tfrac{1}{2} U_s^2 \\
\tilde{\tau}_s &= -\rho_s [\langle \mathbf{W}\mathbf{W} \rangle_s - \tfrac{1}{3}\langle W^2 \rangle_s \mathbf{I}] = \tau_s - \rho_s [\mathbf{U}_s \mathbf{U}_s - \tfrac{1}{3} U_s^2 \mathbf{I}] \\
\tilde{\mathbf{Q}}_s &= \mathbf{Q}_{\text{int},s} + \tfrac{1}{2}\rho_s \langle \mathbf{W}\, W^2 \rangle_s \\
&= \mathbf{Q}_s + [\rho_s (h_s + \tfrac{1}{2} U_s^2)\mathbf{I} - \tau_s]\cdot\mathbf{U}_s
\end{aligned} \tag{9}$$

where $h_s = \epsilon_s + p_s/\rho_s$ is the species enthalpy. Introducing (9) into (7), the following conservation equations are obtained:

$$\begin{aligned}
\frac{\partial \rho_s}{\partial t} + \nabla\cdot(\rho_s \mathbf{w} + \rho_s \mathbf{U}_s) &= S_s \\
\frac{\partial}{\partial t}(\rho_s \mathbf{w} + \rho_s \mathbf{U}_s) + \nabla\cdot(\rho_s \mathbf{w}\mathbf{w} + \mathbf{w}\rho_s \mathbf{U}_s + \rho_s \mathbf{U}_s \mathbf{w} + \tilde{p}_s \mathbf{I}) &= \\
\nabla\cdot\tilde{\tau}_s + \rho_s \mathbf{g} + \zeta_s \mathbf{E} + (\zeta_s \mathbf{w} + \zeta_s \mathbf{U}_s) \times \mathbf{B} + \mathbf{A}_s & \\
\frac{\partial}{\partial t}\left[\rho_s\left(\tilde{\epsilon}_s + \tfrac{1}{2} w^2\right) + \rho_s \mathbf{U}_s\cdot\mathbf{w}\right] & \\
+\nabla\cdot\left[\rho_s \mathbf{w}\left(\tilde{\epsilon}_s + \tfrac{1}{2} w^2\right) + \rho_s \mathbf{U}_s\cdot\mathbf{w}\mathbf{w} + \rho_s \mathbf{U}_s \tfrac{1}{2} w^2 + \tilde{p}_s \mathbf{w}\right] &= \\
\nabla\cdot\left[\tilde{\tau}_s\cdot\mathbf{w} - \tilde{\mathbf{Q}}_s\right] + (\rho_s \mathbf{w} + \rho_s \mathbf{U}_s)\cdot\mathbf{g} + \mathbf{E}\cdot(\zeta_s \mathbf{w} + \zeta_s \mathbf{U}_s) + M_s &
\end{aligned} \tag{10}$$

Define the following overall properties:

$$\begin{aligned}
\epsilon = \sum_s \rho_s \tilde{\epsilon_s}/\rho \quad \zeta = \sum_s \zeta_s \quad \mathbf{J} = \sum_s \zeta_s \mathbf{U}_s \\
p = \sum_s \tilde{p}_s \qquad \tau = \sum_s \tilde{\tau}_s \quad \mathbf{Q} = \sum_s \tilde{\mathbf{Q}}_s
\end{aligned} \tag{11}$$

The terms in (11) are, respectively, the net thermal energy, space charge, conduction current, pressure, viscous stress, and heat flux. The total electrical current is $\mathbf{j} = \zeta\mathbf{w} + \mathbf{J}$. Using these new definitions, and summing (10) over all species, the global conservation laws for mass, momentum, and total energy are obtained:

$$\begin{aligned} \frac{\partial \rho}{\partial t} + \nabla\cdot(\rho\mathbf{w}) &= 0 \\ \frac{\partial}{\partial t}(\rho\mathbf{w}) + \nabla\cdot(\rho\mathbf{w}\mathbf{w} + p\mathbf{I}) &= \nabla\cdot\tau + \rho\mathbf{g} + \zeta\mathbf{E} + \mathbf{j}\times\mathbf{B} \\ \frac{\partial}{\partial t}\left[\rho(\epsilon + \tfrac{1}{2}w^2)\right] + \nabla\cdot\left[\rho\mathbf{w}(\epsilon + \tfrac{1}{2}w^2) + p\mathbf{w}\right] &= \\ \nabla\cdot[\tau\cdot\mathbf{w} - \mathbf{Q}] + \rho\mathbf{w}\cdot\mathbf{g} + \mathbf{E}\cdot\mathbf{j} & \end{aligned} \tag{12}$$

where all the collision source terms have summed to zero. This is a slightly generalized form of Eq. (3).

Note the appearance in Eq. (9) of the diffusion velocity terms that arise from the change of reference frame from that of the species velocity to that of the mass-averaged velocity. If terms of order U_s^2 are neglected, all the quantities except the heat flux are the same in the mass-averaged reference frame as in the species reference frame. For the heat flux we have $\tilde{\mathbf{Q}}_s \approx \mathbf{Q}_s + \rho_s\mathbf{U}_s h_s$, so that the total heat flux becomes $\mathbf{Q} = \sum_s \mathbf{Q}_s + \sum_s \rho_s\mathbf{U}_s h_s$ in this approximation, which is the form used in Eq. (5).

The error introduced by this approximation in the summations of Eq. (11) is small if $\frac{1}{2}\rho_s U_s^2 \ll \rho\epsilon$, in other words for either small diffusion velocities or small mass fractions. This is a good approximation for a weakly-ionized gas, because the neutral particles have high number density but small diffusion velocities, whereas the charged particles have high diffusion velocities but low number densities.

A check of representative values of $\frac{1}{2}\rho_s U_s^2/(\rho\epsilon)$ at a time (10 ns) close the the peak in electric field magnitude in the present calculations illustrates this point. In the numerical solution, this parameter for both ions and electrons has value of about 1×10^{-6} in the plasma. Values for the electrons drop off in the sheath, but the values for the ions peak near the sheath edge, with a maximum of about 2×10^{-3} for N_2^+. Thus the mass-averaged formulation should be accurate for the present calculations, but a careful check is warranted if calculations are carried out for lower density discharges.

Acknowledgments

This project is sponsored in part by the Air Force Office of Scientific Research (monitored by F. Fahroo), and by a grant of High Performance Computing time from the Air Force Research Laboratory Major Shared Resource Center. Work at The Ohio State University was funded in part by the Chief Scientist Innovative Research Fund (CSIRF) of the Air Force Research Laboratory Air Vehicles Directorate (AFRL/RB).

The authors would like to thank M. N. Shneider for helpful discussions, and for pointing out Refs. 22 and 23.

DuPont™ and Kapton® are trademarks or registered trademarks of E. I. du Pont de Nemours and Company.

Cleared for public release, distribution unlimited (88ABW-2011-6358).

References

[1]Kantrowitz, A. R., "A Survey of Physical Phenomena Occurring in Flight at Extreme Speeds," *Proceedings of the Conference on High-Speed Aeronautics*, edited by A. Ferri, N. J. Hoff, and P. A. Libby, Polytechnic Institute of Brooklyn, New York, 1955, pp. 335–339.

[2]Resler, E. L. and Sears, W. R., "The Prospects for Magneto-Aerodynamics," *Journal of the Aeronautical Sciences*, Vol. 25, No. 4, 1958, pp. 235–245,258.

[3]Malik, M., Weinstein, L., and Hussaini, M. Y., "Ion Wind Drag Reduction," AIAA Paper 83-0231.

[4]Roth, J. R., Sherman, D. M., and Wilkinson, S. P., "Electrohydrodynamic Flow Control with a Glow-Discharge Surface Plasma," *AIAA Journal*, Vol. 38, No. 7, 2000, pp. 1166–1172.

[5]Palmer, G., "Magnetic Field Effects on the Computed Flow over a Mars Return Aerobrake," *Journal of Thermophysics and Heat Transfer*, Vol. 7, No. 2, 1993, pp. 294–301.

[6]Gurijanov, E. P. and Harsha, P. T., "AJAX: New Directions in Hypersonic Technology," AIAA Paper 96-4609.

[7]Adamovich, I. V., Subramaniam, V. V., Rich, J. W., and Macheret, S. O., "Phenomenological Analysis of Shock-Wave Propagation in Weakly Ionized Plasmas," *AIAA Journal*, Vol. 36, No. 5, 1998, pp. 816–822.

[8]Poggie, J., "Modeling the Propagation of a Shock Wave Through a Glow Discharge," *AIAA Journal*, Vol. 38, No. 8, 2000, pp. 1411–1418.

[9]Poggie, J. and Gaitonde, D. V., "Magnetic Control of Flow Past a Blunt Body: Numerical Validation and Exploration," *Physics of Fluids*, Vol. 14, No. 5, 2002, pp. 1720–1731.

[10]Gaitonde, D. V. and Poggie, J., "Implicit Technique for Three-Dimensional Turbulent Magnetoaerodynamics," *AIAA Journal*, Vol. 41, No. 11, 2003, pp. 2179–2191.

[11]Adamovich, I. V., Lempert, W. R., Nishihara, M., Rich, J. W., and Utkin, Y. G., "Repetitively Pulsed Nonequilibrium Plasmas for Magnetohydrodynamic Flow Control and Plasma-Assisted Combustion," *Journal of Propulsion and Power*, Vol. 24, No. 6, 2008, pp. 1198–1215.

[12]Poggie, J., "Numerical Simulation of Direct Current Glow Discharges for High-Speed Flow Control," *Journal of Propulsion and Power*, Vol. 24, No. 5, 2008, pp. 916–922.

[13]Adamovich, I. V., Nishihara, M., Choi, I., Uddi, M., and Lempert, W. R., "Energy Coupling to the Plasma in Repetative Nanosecond Pulse Discharges," *Physics of Plasmas*, Vol. 16, 2009, Art. 113505.

[14]Bisek, N., Boyd, I., and Poggie, J., "Numerical Study of Plasma-Assisted Aerodynamic Control for Hypersonic Vehicles," *Journal of Spacecraft and Rockets*, Vol. 46, No. 3, 2009, pp. 568–576.

[15]Bisek, N., Boyd, I., and Poggie, J., "Numerical Study of Magnetoaerodynamic Flow Around a Hemisphere," *Journal of Spacecraft and Rockets*, Vol. 47, No. 5, 2010, pp. 816–827.

[16]Poggie, J., Tilmann, C. P., Flick, P. M., Silkey, J. S., Osborne, B. A., Ervin, G., Maric, D., Mangalam, S., and Mangalam, A., "Closed-Loop Stall Control System," *Journal of Aircraft*, Vol. 47, No. 5, 2010, pp. 1747–1755.

[17]Nishihara, M., Takashima, K., Rich, J. W., and Adamovich, I. V., "Mach 5 Bow Shock Control by a Nanosecond Pulse Surface DBD," AIAA Paper 2011-1144.

[18]Romig, M. F., "The Influence of Electric and Magnetic Fields on Heat Transfer to Electrically Conducting Fluids," *Advances in Heat Transfer*, edited by T. F. Irvine and J. P. Hartnett, Vol. 1, Academic Press, New York, 1964, pp. 267–354.

[19]Samimy, M., Adamovich, I., Webb, B., Kastner, J., Hileman, J., Keshav, S., and Palm, P., "Development and Characterization of Plasma Actuators for High Speed Jet Control," *Experiments in Fluids*, Vol. 37, No. 4, 2004, pp. 577–588.

[20]Roupassov, D. V., Nikipelov, A. A., Nudnova, M. M., and Starikovskii, A. Y., "Flow Separation Control by Plasma Actuator with Nanosecond Pulsed-Periodic Discharge," *AIAA Journal*, Vol. 47, No. 1, 2009, pp. 168–185.

[21]Macheret, S. O., Shneider, M. N., and Miles, R. B., "Modeling of Air Plasma Generation by Repetitive High-Voltage Nanosecond Pulses," *IEEE Transactions on Plasma Science*, Vol. 30, No. 3, 2002, pp. 1301–1314.

[22]Pugh, E. R., Wallace, J., Jacob, J. H., Northam, D. B., and Daugherty, J. D., "Optical Quality of Pulsed Electron-Beam Sustained Lasers," *Applied Optics*, Vol. 13, No. 11, 1974, pp. 2512–2517.

[23]Aleksandrov, V. V., Koterov, V. N., Pustovalov, V. V., Soroka, A. M., and Suchkov, A. F., "Space-Time Evolution of the Cathode Layer in Electron-Beam-Controlled Lasers," *Soviet Journal of Quantum Electronics*, Vol. 8, No. 1, 1978, pp. 59–63.

[24]Unfer, T. and Boeuf, J. P., "Modelling of a Nanosecond Surface Discharge Actuator," *Journal of Physics D: Applied Physics*, Vol. 42, 2009, Art. 194017.

[25]Popov, N. A., "Investigation of the Mechanism for Rapid Heating of Nitrogen and Air in Gas Discharges," *Plasma Physics Reports*, Vol. 27, No. 10, 2001, pp. 886–896.

[26]Nishihara, M., Takashima, K., Rich, J. W., and Adamovich, I. V., "Mach 5 Bow Shock Control by a Nanosecond Pulse Surface Dielectric Barrier Discharge," *Physics of Fluids*, Vol. 23, 2011, Art. 066101.

[27]Lee, S., Goettke, M. K., Loth, E., Tinapple, J., and Benek, J., "Microramps Upstream of an Oblique-Shock / Boundary-Layer Interaction," *AIAA Journal*, Vol. 48, No. 1, 2010, pp. 104–118.

[28]Poggie, J., Bisek, N. J., Adamovich, I. V., and Nishihara, M., "High-Speed Flow Control with Electrical Discharges," AIAA Paper 2011-3104.

[29]Kirpichnikov, A. A. and Starikovskii, A. Y., "Nanosecond Pulse Discharge – Always Uniform?" *IEEE Transactions on Plasma Science*, Vol. 36, No. 4, 2008, pp. 898–899.

[30]Bisek, N., Poggie, J., Nishihara, M., and Adamovich, I., "Computational and Experimental Analysis of Mach 5 Air Flow over a Cylinder with Nanosecond Pulse Discharge," AIAA Paper, January 2012, submitted to the AIAA Aerospace Sciences Meeting.

[31]Uddi, M., Jiang, N., Adamovich, I. V., and Lempert, W. R., "Nitric Oxide Density Measurements in Air and Air/Fuel Nanosecond Pulse Discharges by Laser Induced Fluorescence," *Journal of Physics D: Applied Physics*, Vol. 42, 2009, Art. 075205.

[32]Kossyi, I. A., Kostinsky, A. Y., Matveyev, A. A., and Silakov, V. P., "Kinetic Scheme of the Nonequilibrium Discharge in Nitrogen-Oxygen Mixtures," *Plasma Sources Science and Technology*, Vol. 1, 1992, pp. 207–220.

[33]Huxley, L. G. H. and Crompton, R. W., *The Diffusion and Drift of Electrons in Gases*, Wiley, New York, 1974.

[34]Itikawa, Y., Hayashi, M., Ichimura, A., Onda, K., Sakimoto, K., Takayanagi, K., Nakamura, M., Nishimura, M., and Takayanagi, T., "Cross Sections for Collisions of Electrons and Photons with Nitrogen Molecules," *J. Phys. Chem. Ref. Data*, Vol. 16, 1986, pp. 985–1010.

[35]Itikawa, Y., Ichimura, A., Onda, K., Sakimoto, K., Takayanagi, K., Hatano, Y., Hayashi, M., Nishimura, H., and Tsurubichi, S., "Cross Sections for Collisions of Electrons and Photons with Oxygen Molecules," *J. Phys. Chem. Ref. Data*, Vol. 18, 1989, pp. 23–42.

[36]Popov, N. A., "Fast Gas Heating in a Nitrogen-Oxygen Discharge Plasma: I. Kinetic Mechanism," *Journal of Physics D: Applied Physics*, Vol. 44, 2011, Art. 285201.

[37]Mintoussov, E. I., Pendleton, S. J., Gerbault, F. G., Popov, N. A., and Starikovskaia, S. M., "Fast Gas Heating in Nitrogen-Oxygen Discharge Plasma: II. Energy Exchange in the Afterglow of a Volume Nanosecond Discharge at Moderate Pressures," *Journal of Physics D: Applied Physics*, Vol. 44, 2011, Art. 285202.

[38]Aleksandrov, N. L., Kindysheva, S. V., Nudnova, M. M., and Starikovskiy, A. Y., "Mechanism of Ultra-Fast Heating in a Non-Equilibrium Weakly Ionized Air Discharge Plasma in High Electric Fields," *Journal of Physics D: Applied Physics*, Vol. 43, 2010, Art. 255201.

[39]Takashima (Udagawa), K., Zuzeek, Y., Lempert, W. R., and Adamovich, I. V., "Characterization of Surface Dielectric Barrier Discharge Plasma Sustained by Repetitive Nanosecond Pulses," *Plasma Sources Science and Technology*, Vol. 20, 2011, Art. 055009.

[40]Little, J., Takashima, K., Nishihara, M., Adamovich, I., and Samimy, M., "Separation Control with Nanosecond Pulse Driven Dielectric Barrier Discharge Plasma Actuators," *AIAA Journal*, 2011, Accepted for publication.

[41]Viehland, L. A. and Mason, E. A., "Transport Properties of Gaseous Ions over a Wide Energy Range, IV," *Atomic Data and Nuclear Data Tables*, Vol. 60, 1995, pp. 37–95.

[42]Nelson, D., Benhenni, M., Eichwald, O., and Yousfi, M., "Ion Swarm Data for Electrical Discharge Modeling in Air and Flue Gas Mixtures," *Journal of Applied Physics*, Vol. 94, No. 1, 2003, pp. 96–103.

[43]Mahadevan, S. and Raja, L., "Simulations of Direct-Current Air Glow Discharges at Pressures 1 Torr: Discharge Model Validation," *Journal of Applied Physics*, Vol. 107, 2010, Art. 093304.

[44]White, F. M., *Viscous Fluid Flow*, McGraw-Hill, New York, 2nd ed., 1991.

[45]Surzhikov, S. T. and Shang, J. S., "Two-Component Plasma Model for Two-Dimensional Glow Discharge in Magnetic Field," *Journal of Computational Physics*, Vol. 199, 2004, pp. 437–464.

[46]Deconinck, T., Mahadevan, S., and Raja, L. L., "Simulation of Direct-Current Surface Plasma Discharge Phenomena in High-Speed Flow Actuation," *IEEE Transactions on Plasma Science*, Vol. 35, No. 5, 2007, pp. 1301–1311.

[47]Poggie, J., "High-Order Compact Difference Methods for Glow Discharge Modeling," AIAA Paper 2009-1047.

[48]Poggie, J., "Compact Difference Methods for Discharge Modeling in Aerodynamics," AIAA Paper 2009-3908.

[49]Poggie, J., "Role of Charged Particle Inertia in Pulsed Electrical Discharges," AIAA Paper 2010-1195.

[50]Poggie, J., "High-Order Numerical Methods for Electrical Discharge Modeling," AIAA Paper 2010-4632.

[51]Beam, R. and Warming, R., "An Implicit Factored Scheme for the Compressible Navier-Stokes Equations," *AIAA Journal*, Vol. 16, No. 4, 1978, pp. 393–402.

[52]Morrison, J., "Flux Difference Split Scheme for Turbulent Transport Equations," AIAA Paper 90-5251.

[53]Gaitonde, D. and Shang, J. S., "Accuracy of Flux-Split Algorithms in High-Speed Viscous Flows," *AIAA Journal*, Vol. 31, No. 7, 1993, pp. 1215–1221.

[54]Anderson, W. K., Thomas, J. L., and van Leer, B., "A Comparison of Finite Volume Flux Vector Splittings for the Euler Equations," AIAA Paper 85-0122.

[55]Ventzek, P. L. G., Hoekstra, R. J., and Kushner, M. J., "Two-Dimensional Modeling of High Plasma Density Inductively Coupled Sources for Materials Processing," *Journal of Vacuum Science and Technology B*, Vol. 12, No. 1, 1994, pp. 461–477.

[56]Holst, T. L., "Transonic Flow Computations Using Nonlinear Potential Methods," *Progress in Aerospace Sciences*, Vol. 36, 2000, pp. 1–61.

[57]Cheney, W. and Kincaid, D., *Numerical Mathematics and Computing*, Brooks/Cole Publishing, Pacific Grove, California, 3rd ed., 1994.

[58]Liepmann, H. W. and Roshko, A., *Elements of Gasdynamics*, J. Wiley, New York, 1957.

[59]Nachbar, W., Williams, F., and Penner, S. S., "The Conservation Equations for Independent Coexistent Continua and for Multicomponent Reacting Gas Mixtures," *Quarterly Journal of Applied Mathematics*, Vol. 17, No. 1, 1959, pp. 43–54.

[60]Chapman, S. and Cowling, T. G., *The Mathematical Theory of Non-Uniform Gases*, Cambridge University Press, 2nd ed., 1952.

[61]Seshadri, S. R., *Fundamentals of Plasma Physics*, Elsevier, New York, 1973.

[62]Olejniczak, J. and Candler, G. V., "Vibrational Energy Conservation with Vibration-Dissociation Coupling: General Theory and Numerical Studies," *Physics of Fluids*, Vol. 7, No. 7, 1995, pp. 1764–1774.

No.	Species	h^0 (eV/particle)
1	N_2	0
2	O_2	0
3	O	2.58
4	O_3	1.48
5	NO	0.93
6	N	4.90
7	$O(^1D)$	2.0
8	$N_2(A^3\Sigma)$	6.17
9	$N_2(B^3\Pi)$	7.35
10	$N_2(a'^1\Sigma)$	8.40
11	$N_2(C^3\Pi)$	11.0
12	e^-	0
13	N_2^+	16.36
14	O^+	16.26
15	O_2^+	12.70

Table 1. Species incorporated in kinetic model.

No.	Reaction	Rate Expression	Coefficients
1	$N_2 + e^- \rightarrow N_2^+ + e^- + e^-$	$\log_{10} k = A + B/(E/N)$	-7.76, -37.0 (-7.17, -61.1)
2	$O_2 + e^- \rightarrow O_2^+ + e^- + e^-$	$\log_{10} k = A + B/(E/N)$	-8.34, -30.7 (-7.42, -71.0)
3	$O_2 + e^- \rightarrow O + O^+ + e^- + e^-$	$\log_{10} k = A + B/(E/N)$	-7.94, -32.2 (-7.78, -35.2)
4	$N_2 + e^- \rightarrow N_2(A^3\Sigma) + e^-$	$\log_{10} k = A + B/(E/N)$	-8.57, -11.3 (-9.06, 15.3)
5	$N_2 + e^- \rightarrow N_2(B^3\Pi) + e^-$	$\log_{10} k = A + B/(E/N)$	-7.97, -13.2 (-8.14, -3.42)
6	$N_2 + e^- \rightarrow N_2(C^3\Pi) + e^-$	$\log_{10} k = A + B/(E/N)$	-7.82, -22.0 (-7.45, -37.0)
7	$N_2 + e^- \rightarrow N_2(a'^1\Sigma) + e^-$	$\log_{10} k = A + B/(E/N)$	-8.15, -15.8 (-8.12, -15.6)
8	$N_2 + e^- \rightarrow N + N + e^-$	$\log_{10} k = A + B/(E/N)$	-7.96, -22.7 (-7.34, -50.2)
9	$O_2 + e^- \rightarrow O + O + e^-$	$\log_{10} k = A + B/(E/N)$	-8.31, -8.40 (-8.63, 7.10)
10	$O_2 + e^- \rightarrow O + O(^1D) + e^-$	$\log_{10} k = A + B/(E/N)$	-7.86, -17.2 (-7.42, -37.1)
11	$N + O_2 \rightarrow NO + O$	$k = AT^n \exp(-E_a/T)$	0.110E-13, 1.00, 3150.
12	$N + NO \rightarrow N_2 + O$	$k = AT^n$	0.105E-11, 0.50
13	$O + O_3 \rightarrow O_2 + O_2$	$k = A\exp(-E_a/T)$	0.200E-10, 2300.
14	$O + O + N_2 \rightarrow O_2 + N_2$	$k = A\exp(-E_a/T)$	0.276E-33, -720.
15	$O + O + O_2 \rightarrow O_2 + O_2$	$k = AT^n$	0.245E-30, -0.63
16	$O + O_2 + N_2 \rightarrow O_3 + N_2$	$k = AT^n$	0.558E-28, -2.00
17	$O + O_2 + O_2 \rightarrow O_3 + O_2$	$k = AT^n$	0.861E-30, -1.25
18	$N_2(A^3\Sigma) + O_2 \rightarrow N_2 + O + O$	$k = 0.170$E-11	
19	$N_2(A^3\Sigma) + O_2 \rightarrow N_2 + O_2$	$k = 0.750$E-12	
20	$N_2(A^3\Sigma) + O \rightarrow N_2 + O(^1D)$	$k = 0.300$E-10	
21	$N_2(A^3\Sigma) + N_2(A^3\Sigma) \rightarrow N_2 + N_2(B^3\Pi)$	$k = 0.770$E-10	
22	$N_2(A^3\Sigma) + N_2(A^3\Sigma) \rightarrow N_2 + N_2(C^3\Pi)$	$k = 0.160$E-09	
23	$N_2(B^3\Pi) + N_2 \rightarrow N_2(A^3\Sigma) + N_2$	$k = 0.300$E-10	
24	$N_2(B^3\Pi) \rightarrow N_2(A^3\Sigma)$	$k = 0.150$E+06	
25	$N_2(B^3\Pi) + O_2 \rightarrow N_2 + O + O$	$k = 0.300$E-09	
26	$N_2(a'^1\Sigma) + N_2 \rightarrow N_2 + N_2$	$k = 0.200$E-12	
27	$N_2(a'^1\Sigma) + O_2 \rightarrow N_2 + O + O(^1D)$	$k = 0.281$E-10	
28	$N_2(C^3\Pi) + N_2 \rightarrow N_2(B^3\Pi) + N_2$	$k = 0.100$E-10	
29	$N_2(C^3\Pi) \rightarrow N_2(B^3\Pi)$	$k = 0.300$E+08	
30	$N_2(C^3\Pi) + O_2 \rightarrow N_2(A^3\Sigma) + O + O$	$k = 0.301$E-09	
31	$O(^1D) + N_2 \rightarrow O + N_2$	$k = 0.257$E-10	
32	$O(^1D) + O_2 \rightarrow O + O_2$	$k = 0.400$E-10	
33	$O^+ + O_2 \rightarrow O_2^+ + O$	$k = 0.199$E-10	
34	$N_2^+ + O_2 \rightarrow N_2 + O_2^+$	$k = 0.600$E-10	
35	$N_2^+ + e^- \rightarrow N + N$	$k = AT_e^n$	0.831E-05, -0.50
36	$O_2^+ + e^- \rightarrow O + O$	$k = AT_e^n$	0.599E-04, -1.00
37	$N_2^+ + e^- + e^- \rightarrow N_2 + e^-$	$k = AT_e^n$	0.140E-07, -4.50
38	$O_2^+ + e^- + e^- \rightarrow O_2 + e^-$	$k = AT_e^n$	0.140E-07, -4.50
39	$O^+ + e^- + e^- \rightarrow O + e^-$	$k = AT_e^n$	0.140E-07, -4.50
40	$N_2^+ + e^- + M \rightarrow N_2 + M$	$k = AT_e^n$	0.312E-22, -1.50
41	$O_2^+ + e^- + M \rightarrow O_2 + M$	$k = AT_e^n$	0.312E-22, -1.50
42	$O^+ + e^- + M \rightarrow O + M$	$k = AT_e^n$	0.312E-22, -1.50

Table 2. Reaction mechanism. Units consistent with number densities in cm^{-3}, and temperatures in K, reduced electric field in 1×10^{-16} V cm^2 (10 Td), one-body rates in s^{-1}, two-body rates in cm^3/s, and three-body rates in cm^6/s. Values in parentheses are alternative curve fits for $E/N > 50 \times 10^{-16}$ V cm^2 ($E/N > 500$ Td).

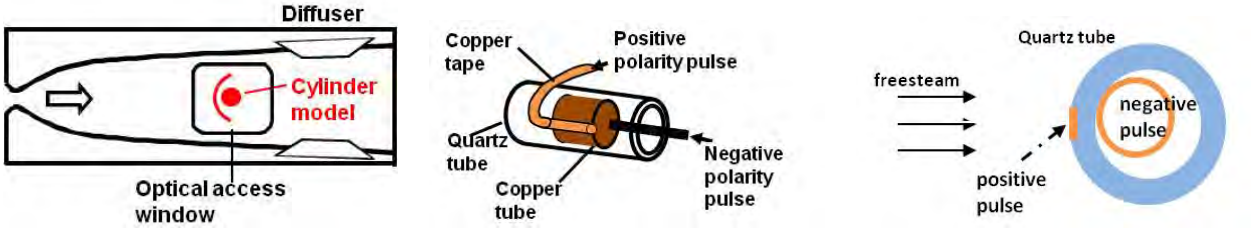

(a) Diagram of cylinder mounted in wind tunnel.

(b) Perspective view of cylinder model.

(c) Side view of cylinder model.

Figure 1. Configuration of Mach 5 cylinder flow experiment.

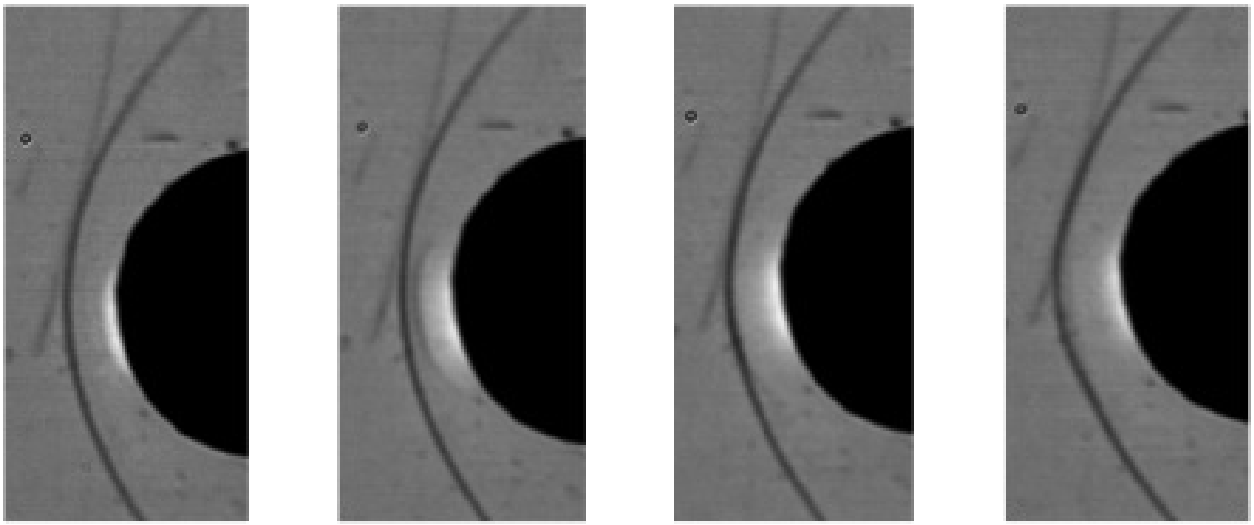

(a) Time: 1 μs.

(b) Time: 2 μs.

(c) Time: 3 μs.

(d) Time: 4 μs.

Figure 2. Side-view schlieren images of Mach 5 cylinder flow perturbed by pulsed discharge.

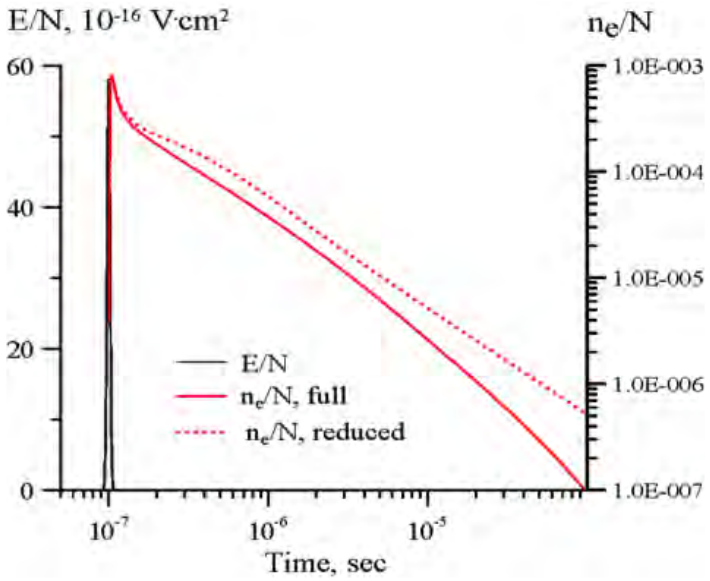

Figure 3. Reduced electric field during the pulse; ionization fraction predicted by the full and reduced air plasma models. Conditions: $p = 30$ Torr, $T_0 = 300$ K, discharge energy loading 100 meV/molecule.

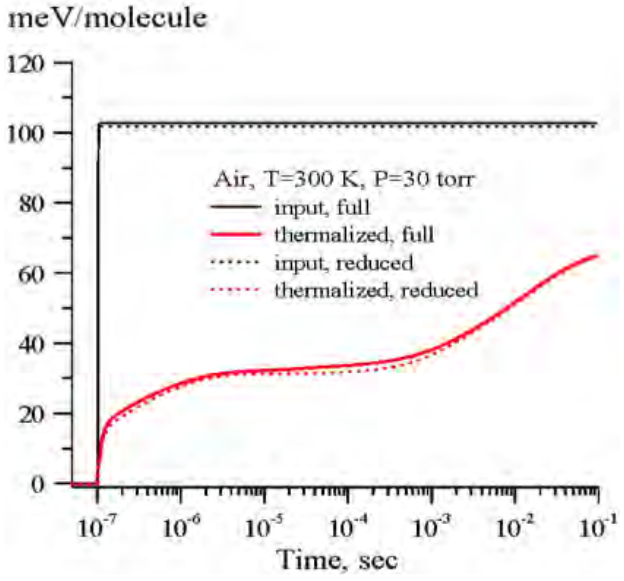

Figure 4. Input pulse energy and energy thermalized after the pulse predicted by the full and reduced air plasma models at the conditions of Fig. 3 ($p = 30$ Torr, $T_0 = 300$ K, 100 meV/molecule).

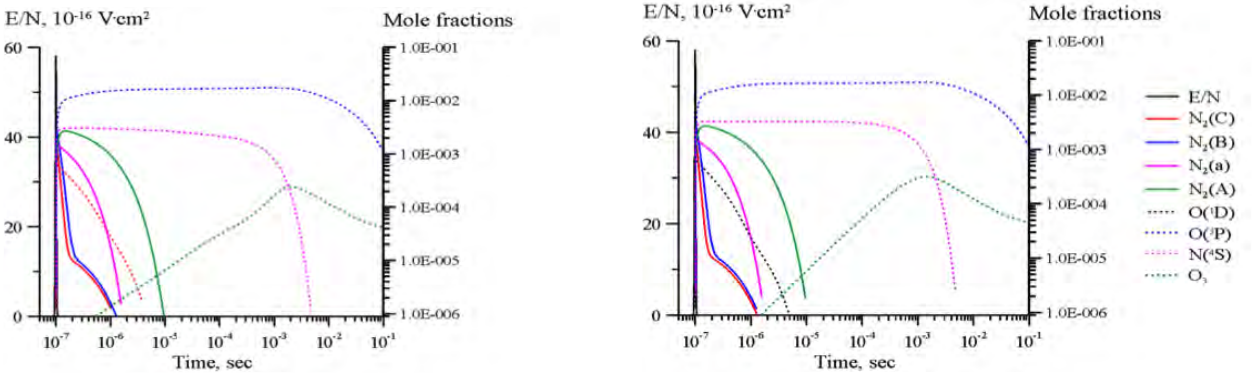

(a) Full kinetic model.

(b) Reduced kinetic model.

Figure 5. Mole fractions of dominant neutral species at the conditions of Fig. 3 (p = 30 Torr, T_0 = 300 K, 100 meV/molecule).

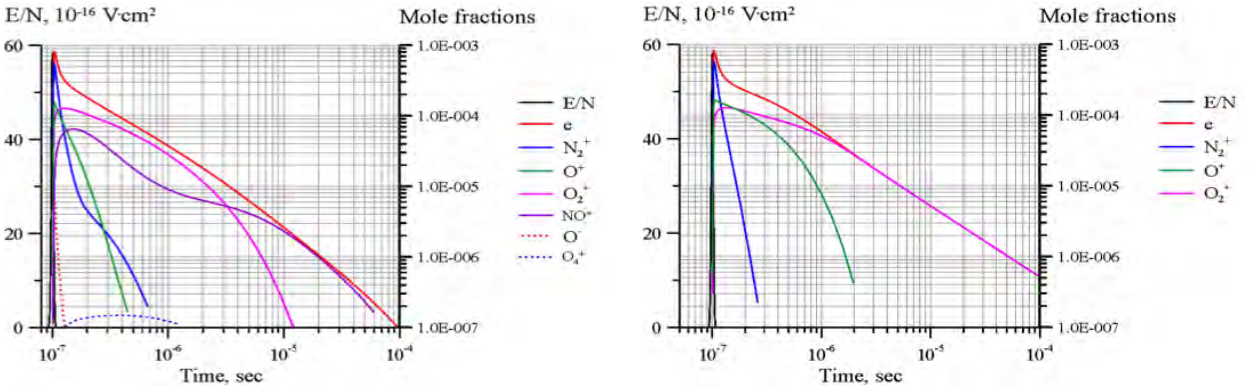

(a) Full kinetic model.

(b) Reduced kinetic model.

Figure 6. Mole fractions of dominant charged species at the conditions of Fig. 3 (p = 30 Torr, T_0 = 300 K, 100 meV/molecule).

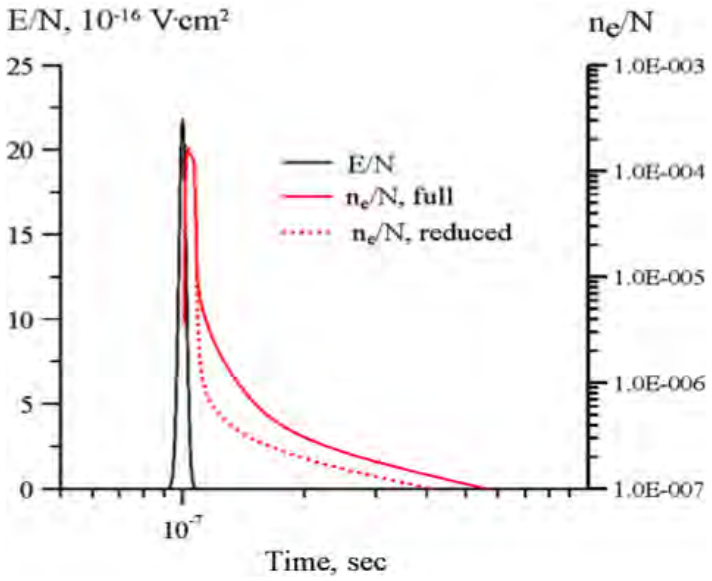

Figure 7. Reduced electric field during the pulse; ionization fraction predicted by the full and reduced air plasma models. Conditions: $p = 760$ Torr, $T_0 = 300$ K, discharge energy loading 130 meV/molecule.

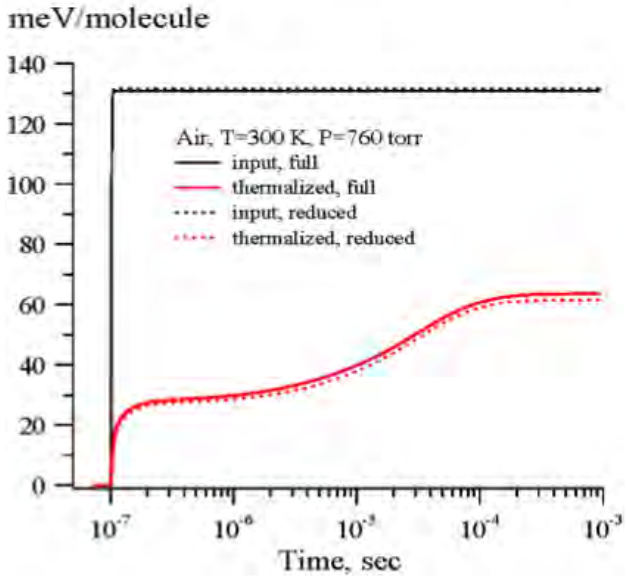

Figure 8. Input pulse energy and energy thermalized after the pulse predicted by the full and reduced air plasma models at the conditions of Fig. 7 ($p = 760$ Torr, $T_0 = 300$ K, 130 meV/molecule).

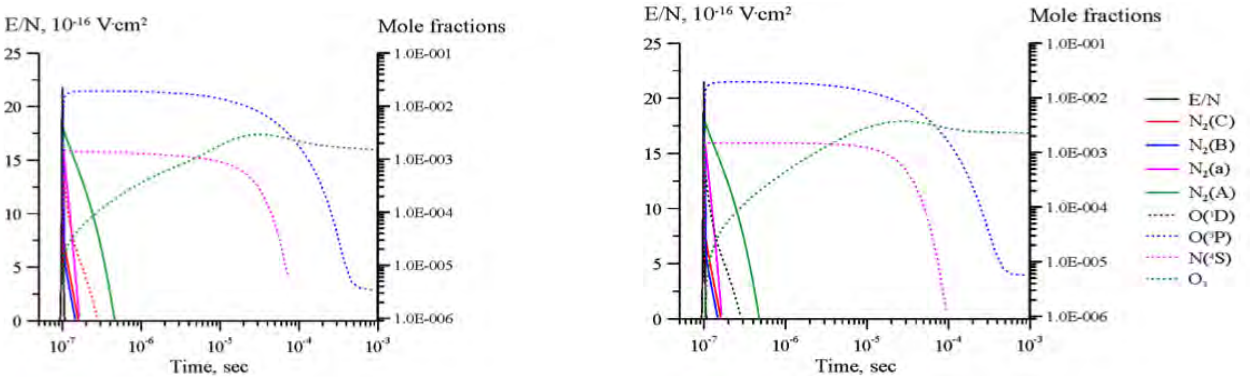

(a) Full kinetic model.

(b) Reduced kinetic model.

Figure 9. Mole fractions of dominant neutral species at the conditions of Fig. 7 (p = 760 Torr, T_0 = 300 K, 130 meV/molecule).

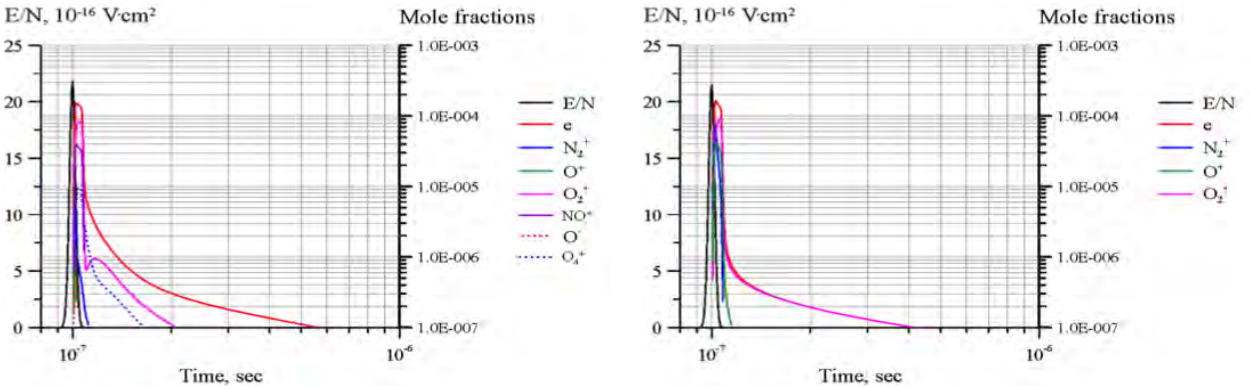

(a) Full kinetic model.

(b) Reduced kinetic model.

Figure 10. Mole fractions of dominant charged species at the conditions of Fig. 7 (p = 760 Torr, T_0 = 300 K, 130 meV/molecule).

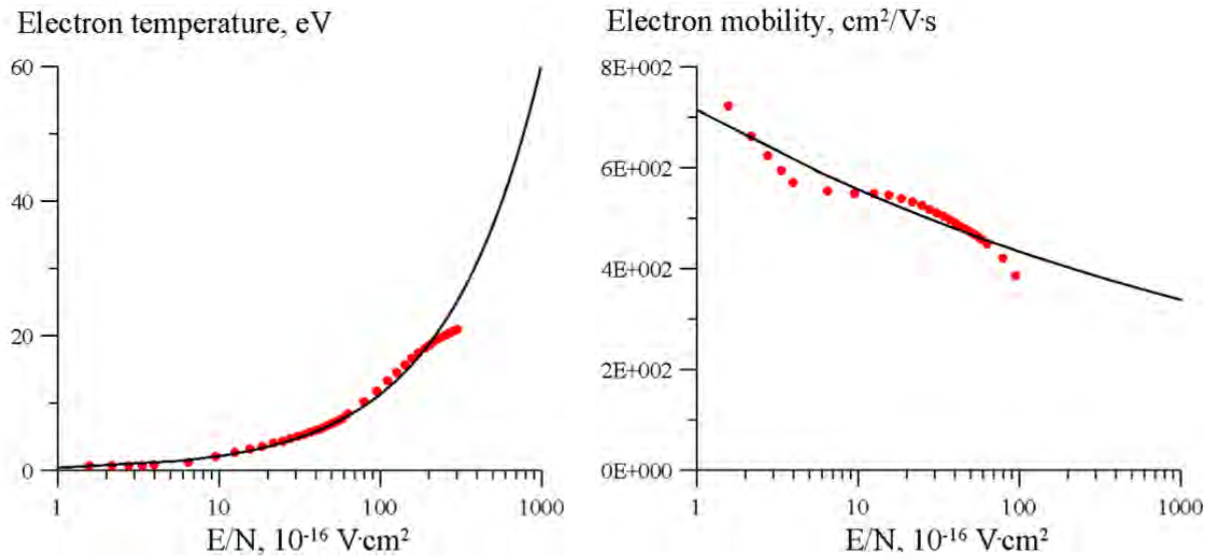

(a) Electron temperature.

(b) Electron mobility at atmospheric pressure ($N = 2.4 \times 10^{19}$ cm^{-3}).

Figure 11. Electron properties as a function of reduced electric field. Lines: curve fits; points: data from Boltzmann equation solutions.

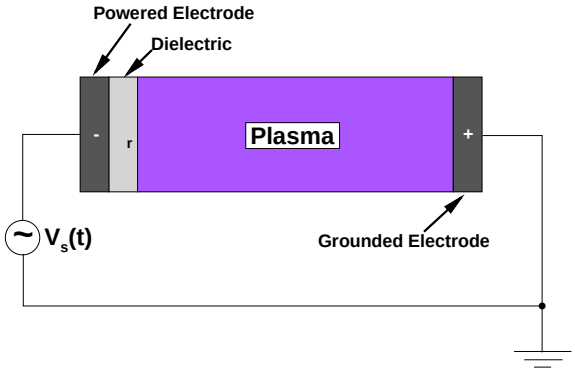

Figure 12. Diagram of computational domain.

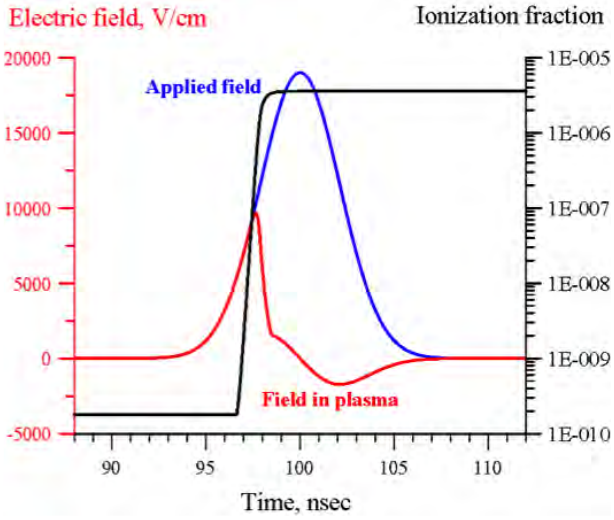

(a) Electric field and ionization fraction, analytical model.

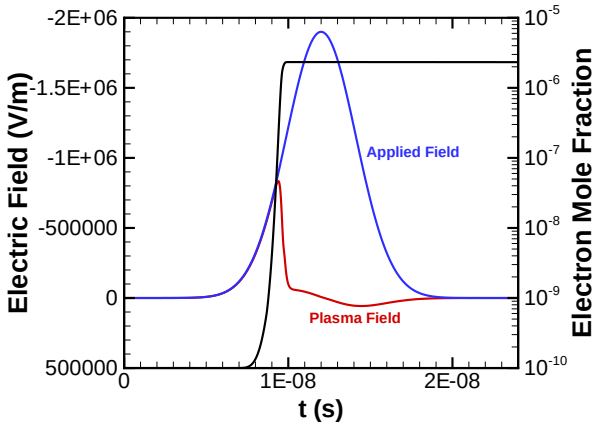

(b) Electric field and ionization fraction, 1-D computations ($x = 8$ mm).

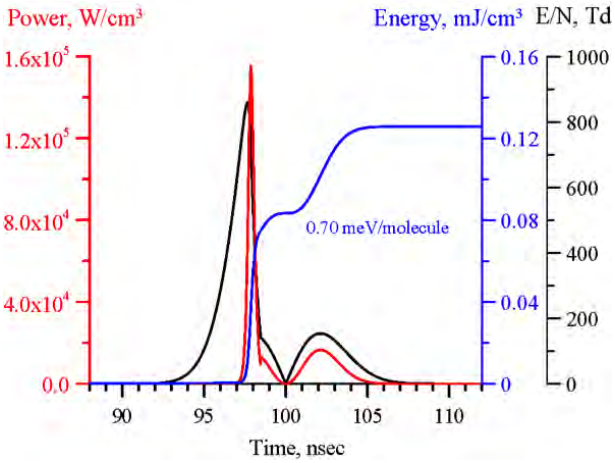

(c) Reduced electric field, power, and thermalized energy, analytical model.

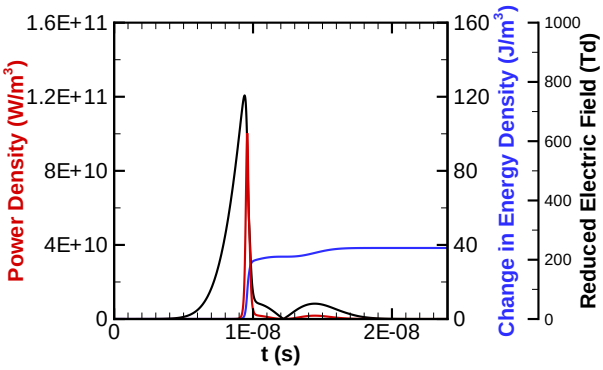

(d) Reduced electric field E/N, dissipated power $\mathbf{E} \cdot \mathbf{J}$, and change in internal energy $\Delta(\rho\epsilon)$, 1-D computations ($x = 8$ mm).

Figure 13. Comparison of analytical model[13] to one-dimensional computations for a station in the quasi-neutral plasma.

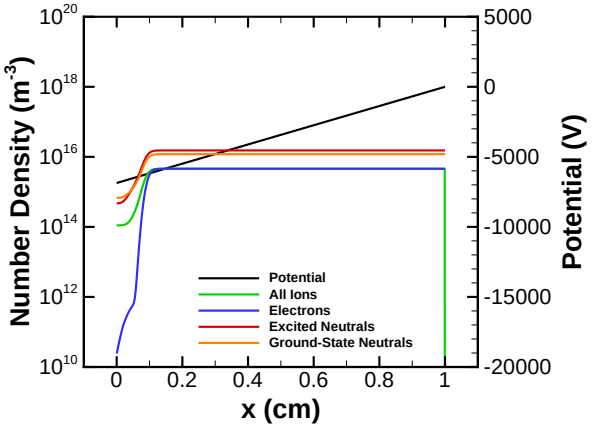

(a) Time: 9 ns.

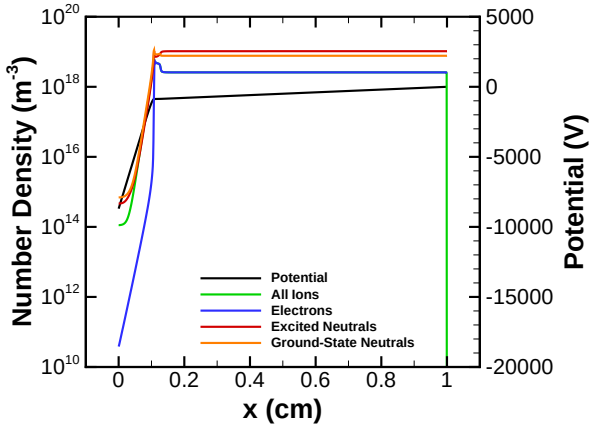

(b) Time: 10 ns.

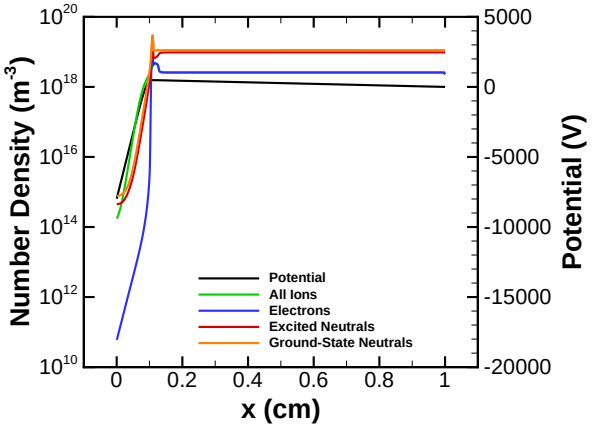

(c) Time: 14 ns.

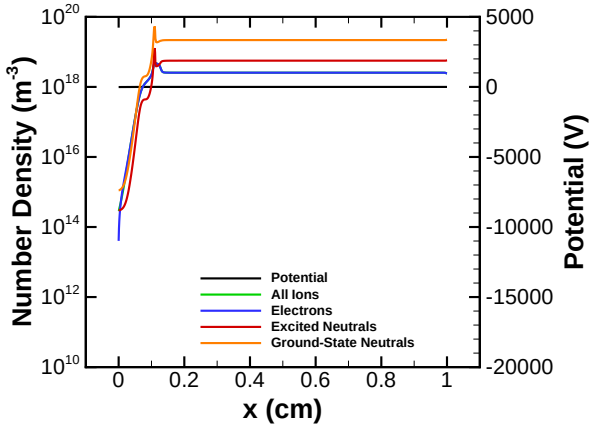

(d) Time: 100 ns.

Figure 14. Discharge profiles predicted by the numerical computations. Ions: N_2^+ , O_2^+, and O^+; electrons: e^-; excited neutrals: $N_2(A^3\Sigma)$, $N_2(B^3\Pi)$, $N_2(a'^1\Sigma)$, $N_2(C^3\Pi)$, and $O(^1D)$; ground-state neutrals: O, O_3, NO, N.

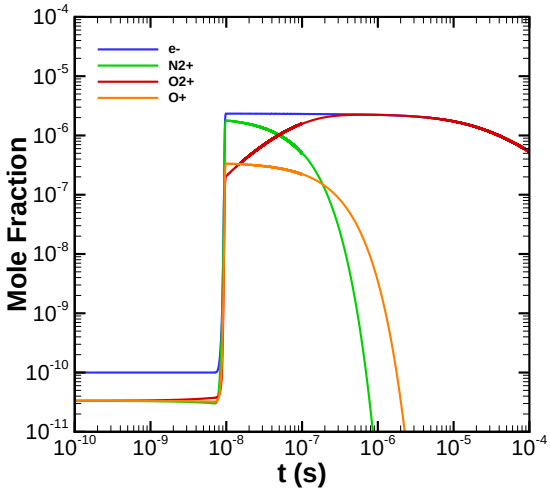

(a) Charged particles: N_2^+ , O_2^+, O^+, and e^-.

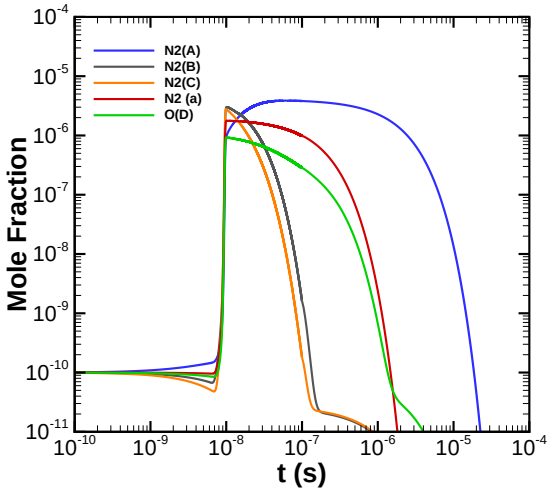

(b) Electronically excited neutrals: $N_2(A^3\Sigma)$, $N_2(B^3\Pi)$, $N_2(a'^1\Sigma)$, $N_2(C^3\Pi)$, and $O(^1D)$.

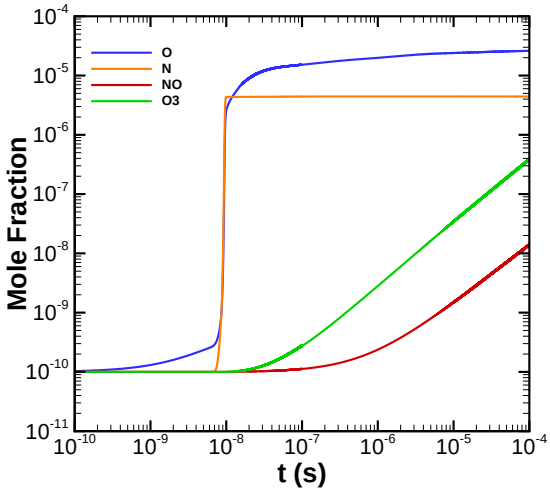

(c) Ground-state neutrals: O, O_3, NO, N.

Figure 15. Time history of species mole fraction in the plasma ($x = 8$ mm). The calculations switch from the full model to the neutral, zero-field model at 1×10^{-7}s.

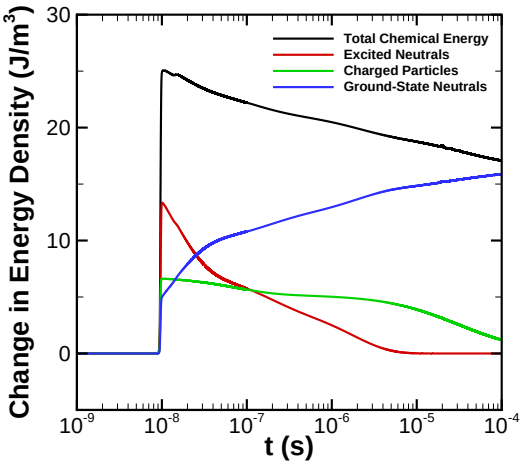

(a) Distribution of chemical energy density over different groups of species. (Plasma, $x = 8$ mm.)

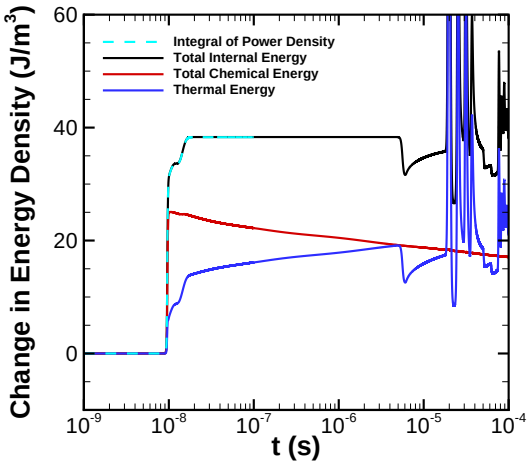

(b) Distribution of energy between chemical and thermal modes. (Plasma, $x = 8$ mm.) Spikes in thermal energy correspond to acoustic wave motion.

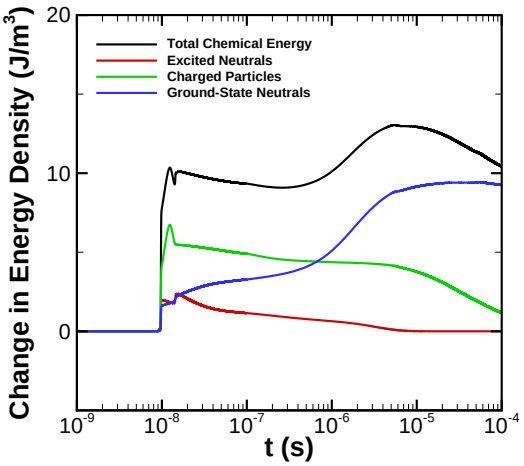

(c) Distribution of chemical energy density over different groups of species. (Sheath, $x = 1$ mm.)

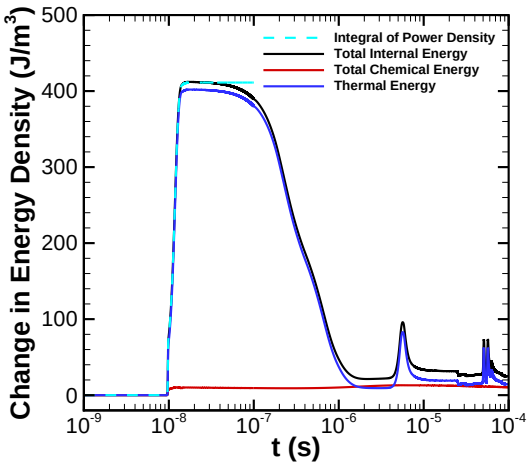

(d) Distribution of energy between chemical and thermal modes. (Sheath, $x = 1$ mm.) Spikes in thermal energy correspond to acoustic wave motion.

Figure 16. Distribution of energy in the plasma and in the sheath. Charged particles: N_2^+ , O_2^+, O^+, and e^-; excited neutrals: $N_2(A^3\Sigma)$, $N_2(B^3\Pi)$, $N_2(a'^1\Sigma)$, $N_2(C^3\Pi)$, and $O(^1D)$; ground-state neutrals: O, O_3, NO, N; change in energy density $\Delta(\rho\epsilon)$, integrated power $\int_0^t \mathbf{E}\cdot\mathbf{J}\, d\hat{t}$. The calculations switch from the full model to the neutral, zero-field model model at 1×10^{-7}s.

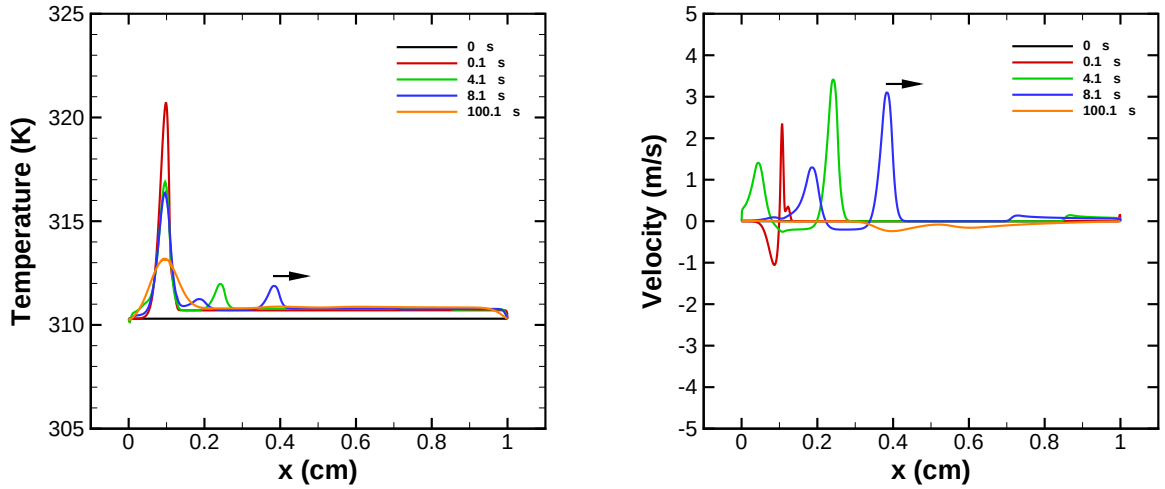

(a) Temperature.

(b) Velocity.

Figure 17. Profiles of the properties of the bulk gas for selected times in the simulation. Arrows indicate the direction of wave motion.